Modelled dynamics of floating and grounded icebergs, with application to the Amundsen Sea

Yavor Kostov[1], Paul R. Holland[1], Kelly A. Hogan[1], James A. Smith[1], Nicolas C. Jourdain[2], Pierre Mathiot[2], Anna Olivé Abelló[2], Andrew H. Fleming[1], Andrew J. S. Meijers[1].

[1]British Antarctic Survey, Cambridge, UK
[2]Univ. Grenoble Alpes/CNRS/IRD/G-INP/INRAE, Institut des Géosciences de l'Environnement, Grenoble, France

Correspondence to: Yavor Kostov (yastov@bas.ac.uk)

Abstract. Icebergs that ground on the submarine Bear Ridge in the Amundsen Sea are known to block the drift of sea ice, playing a crucial role in maintaining shelf sea ocean conditions. This important iceberg—sea ice—ocean interaction is ubiquitous around the Antarctic shelf seas. To better represent the drift, grounding, and ungrounding of icebergs in the vicinity of such seabed ridges, we introduce new dynamics into the iceberg component of the Nucleus for European Modelling of the Ocean (NEMO) ocean general circulation model. The pre-existing iceberg capability in NEMO did not facilitate iceberg grounding, but here we implement a physically-motivated grounding scheme with parameter choices guided by observations from the Amundsen Sea. When the bergs are grounded, they now experience bottom sediment resistance, bedrock friction, and an acceleration due to gravity acting down topographic slopes. We also improve the representation of ocean turbulent drag and ocean pressure gradients, both for freely-floating and grounded icebergs, by incorporating the depth-dependence of these forces. We examine the diverse set of forces acting on simulated icebergs in the Amundsen Sea, and compare our simulations with iceberg observations near Bear Ridge. The new iceberg physics pave the way for future studies to explore the existence of possible feedback mechanisms between iceberg grounding, changing sea ice and ocean conditions, and iceberg calving from the ice shelves.

1 Introduction

Icebergs play a major role in the redistribution of freshwater in the polar oceans, contributing roughly half of the freshwater discharge from Antarctica and Greenland (Cendese and Straneo, 2022; Davison et al., 2023). Compared to basal melt of ice shelves, which causes localized freshening, icebergs tend to release meltwater farther offshore (Merino et al., 2016; Fox-Kemper et al, 2019). At the same time, there is diversity in the freshwater contribution among icebergs of different dimensions; large tabular bergs may become grounded in shallow shelf seas shortly after they calve and hence release melt water closer to the shore (Cenedese and Straneo, 2022; Olivé Abelló et al., in prep.). Nevertheless, the largest icebergs have the longest life-span, allowing for a sustained contribution of meltwater (Cenedese and Straneo, 2022). Stern et al. (2016) and Fox-Kemper et al. (2019) point out that modelling the behaviour of the largest icebergs is particularly challenging.

Icebergs of all sizes are important not only for the thermodynamics of the polar oceans, but also for marine biology and ecology. For example, iceberg debris is a significant source of silica, whose supply to the ocean enhances the biological carbon pump by promoting the growth of diatom phytoplankton populations (Hawkings et al., 2017). Cefareli et al. (2016) identify diatom species attached to the submerged parts of iceberg walls, providing further evidence for the biological relevance of icebergs. Tarling et al. (2024) argue that icebergs impact the distribution of phytoplankton and particulate matter via changes in the salinity-driven stratification, while Lucas et al. (2024) suggest that iceberg melting allows for deep nutrient-rich water to penetrate layers shallower than the stratification maximum. The latter promotes primary production and hence, the carbon pump (Smith et al., 2007; Cenedese and Streaneo, 2022; Lucas et al., 2024). Last but not least, icebergs also represent one of the largest sources of iron in the polar ocean, while at the same time they are also very heterogeneous and variable in their iron content (Hopwood et al., 2019).

40   As they drift, icebergs may run into topographic obstacles or plough into seafloor sediment, a phenomenon that has

41   been the subject of scientific inquiry as far back as the 19th century, when Charles Darwin published a short communication

42   on iceberg interaction with the ocean bottom (Darwin 1855). More recently, a number of studies on iceberg scouring have had

43   a focus on protecting underwater infrastructure (e.g., Chari 1979; Chari et al., 1980; and Lopez et al., 1981).

44   Topographic blocking by grounded icebergs can also significantly modify regional ocean conditions (Nakayama et

45   al., 2014; St-Laurent et al., 2015; St-Laurent et al., 2024). Bett et al. (2020) suggest the importance of iceberg grounding along

46   Bear Ridge in the Amundsen Sea, Antarctica (Figure 1; Mazur et al., 2019) to the oceanography of the region. Icebergs

47   grounded on Bear Ridge form a physical barrier to westward sea ice transport, creating a dipole in the sea-ice concentration.

48   Icebergs blocking the supply of drifting sea ice creates the Amundsen Sea Polynya to the west of Bear Ridge, which has a

49   strong cooling effect on the water column and is important to the biological productivity of the region (e.g., Arrigo et al.,

50   2012). To the east of Bear Ridge, icebergs blocking the export of sea ice suppresses polynya activity, reducing the local

51   formation of Winter Water and thereby promoting the intrusion of warmer modified Circumpolar Deep Water (mCDW; Bett

52   et al., 2020). The drift and grounding of icebergs in the Amundsen Sea is shown in the Supplementary Movie in Appendix A

53   (Kostov et al., 2025a, an update of the supplementary movie in Bett et al., 2020), which contains Copernicus Sentinel-1 SAR

54   (synthetic aperture radar) images taken over the time period 2017-2024. The impact on sea ice in the region is also clearly

55   visible.

56   Crucially, these dynamics offer the possibility of a local positive feedback loop. The warm mCDW on the shelf in the

57   Amundsen Sea supports rapid melting of the surrounding ice shelves (Jacobs et al 2012; Dutrieux et al, 2014). Changes in the

58   supply of warm CDW has led to rapid thinning and acceleration of these ice shelves and their tributary ice streams (Mouginot

59   et al., 2016; Shepherd et al., 2019; Naughten et al., 2022). This has caused an overall increase in iceberg calving, punctuated

60   by several large ice shelf collapse events that released large numbers of icebergs (Miles et al., 2020; Joughin et al., 2021,

61   Davison et al., 2023). Changes in the supply of icebergs to Bear Ridge (and the thickness of those bergs) could affect the

62   characteristics of the grounded iceberg wall, influencing sea ice blocking, hence CDW temperatures, and ultimately ice shelf

63   melting and calving (Bett et al., 2020). The sign and strength of this feedback mechanism and its future response to projected

64   climate change are unknown and have important implications for the sea-level contribution from the West Antarctic Ice Sheet.

65   These important roles of icebergs in the climate system necessitate their proper representation in ocean models (Fox-

66   Kemper et al, 2019). Some of the earliest efforts in modelling iceberg trajectories are attributed to Bigg et al. (1997) and

67   Gladstone et al. (2001). Martin and Adcroft (2010) introduce icebergs in a fully coupled climate model, and Marsh et al. (2015)

68   pioneer the first version of the iceberg module in the state-of-the-art Nucleus for European Modelling of the Ocean (NEMO-

69   v4.2.0) ocean model (Madec, G. and NEMO-Team, 2016; Madec, G. and NEMO Systems Team, 2022). Bigg et al. (2018) use

70   NEMO to model iceberg hazard, while Merino et al. (2016) further develop the representation of icebergs in NEMO and, more

71   specifically, simulate the impact of depth-varying ocean properties on iceberg dynamics and thermodynamics.

72   In this study, we introduce a new physically and observationally motivated iceberg grounding capability in NEMO.

73   This is particularly designed and tuned for the Amundsen Sea, given the importance of icebergs grounding on Bear Ridge, but

74   the underlying physics should be generally applicable. Sequences of satellite images from the Amundsen Sea region reveal

75   complex patterns of iceberg motion near Bear Ridge with multiannual episodes of iceberg grounding (see the Supplementary

76   Movie). Seafloor records of iceberg scours collected from multibeam bathymetry sounding in the vicinity of Bear Ridge also

77   reflect the dynamics that arise from the combination of multiple forces acting on a grounded berg. A compilation of sediment

78   density and shear strength data from representative sediment cores in the Amundsen Sea point to the important role that the

79   so-called 'silt resistance' (Chari, 1979; hereafter referred to as 'sediment resistance') may play for the deceleration and arrest

80   of grounded icebergs. These various observations, along with theoretical analysis of the underlying physical principles behind

81   iceberg motion, inform our improvements to the NEMO iceberg module. This paper first develops the physical principles

82   controlling the grounding of icebergs in NEMO, before applying these new physics in a regional model of the Amundsen Sea.

83

84

85
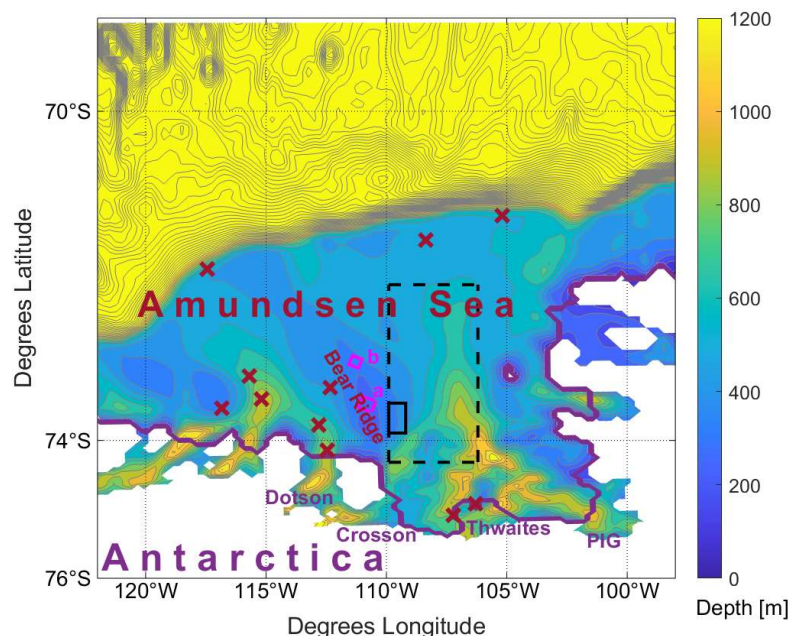
Figure 1: Amundsen Sea and Bear Ridge topography [m] based on the BedMachine Antarctica dataset (Morlighem et al., 2020) and
re-gridded on the model configuration grid. Gray contours are spaced 80 m apart. Magenta contours delimit the bounds of boxes a
and b in Figure 2, indicating the sites of observed iceberg scours in Section 2.1 with magenta labels matching boxes a and b in Figure
2. Dark red crosses mark the locations of sediment samples analysed in Section 2.2. The thick purple line shows the ice shelf edge,
with major ice shelves labelled: Dotson, Crosson, Thwaites, and Pine Island Glacier (PIG). Solid (dashed) black lines show the
boundaries of the boxes where icebergs are released in the SHORT (LONG) simulations.

92   In Section 2 we present and discuss observations of iceberg scouring and sediment properties in the Amundsen Sea.

93   In Section 3, we describe the theoretical and modelling advances for iceberg dynamics and grounding and their implementation

94   in NEMO. In Section 4 we test our modelling developments in an Amundsen Sea regional configuration of NEMO and we

95   describe the force balance of freely floating vs grounded icebergs. In Section 5 we summarise the results of our observationally-

96   motivated numerical simulations with the updated NEMO model and then conclude.

97   **2 Seafloor morphology and sediment properties in the Amundsen Sea**

98   **2.1 Observed iceberg scours**

99   Iceberg scours (also called ploughmarks) are widespread on the seafloor in the Amundsen Sea, where they are present in two

100   settings. First, they are extensive across the middle—outer continental shelf where water depths shoal sufficiently to have

101   allowed icebergs to touch the seabed (<~700 m), and second, they occur on the shallow banks between the landward-deepening

102   glacial troughs that cross the continental shelf (Figure 1). Scour populations are dominated by single-keeled v- or u-shaped

103   forms with relatively small widths and incision depths, although a few multi-keeled forms are present. A comprehensive

104   morphometric study of >10,800 scours in Pine Island Trough (East) by Wise et al. (2017) returned average single-keel scour

105   widths and depths of 115 m and 2.8 m, respectively (ranges were 12-449 m and 0.1-22 m). Further west, on the banks around

106   the Dotson-Getz glacial trough, typical scour widths and depths are 100-250 m and 4-10 m, respectively (Graham et al., 2009).

107   Most of the scours in deeper water (> 700 m) on the middle-outer shelf are likely to be relict forms incised during the

108   last deglaciation, given the keel depths of modern iceberg populations and bathymetric impediments on the inner shelf

3

109   (Dowdeswell & Bamber, 2007; Wise et al., 2017). In contrast, satellite imagery from the last decade shows clear accumulations

110   of modern icebergs on the shallow banks to the west of calving glaciers in the eastern Amundsen Sea (see Supplementary

111   Movie in Appendix A). After they are calved, the icebergs are moved westwards by prevailing winds and ocean currents and

112   run aground wherever water depths shallow significantly. Bear Ridge, a N/NW-trending remnant of crystalline basement (Gohl

113   et al., 2013) with water depths of 150-450 m, exhibits one of the most persistent collections of grounded icebergs today on its

114   eastern margin, with icebergs of all sizes running aground there (Mazur et al., 2019). Here, we manually map more than 60

115   scours from existing multibeam-bathymetric data on the eastern flank and central part of Bear Ridge as a representative

116   population of modern scours. We describe their morphology qualitatively with the aim of characterising modern iceberg

117   grounding events, and then we provide metrics on their dimensions to calibrate the modelled scouring in Section 4.

118   Multibeam-bathymetric data from 17 research cruises with tracks across Bear Ridge were gridded with 30-m square

119   grid cells and visualised in ArcGIS Pro 3.3.1 and QPS Fledermaus 8.6.1 for analysis. More than 60 iceberg scours were

120   mapped, visualised with hillshading, and their cross-sectional widths and depths measured. Overall metrics are presented in

121   Table 1.

122   Iceberg scours on Bear Ridge exhibit a variety of forms (Figure 2). Many incisions consist of single v- to u-shaped

123   curvilinear depressions with shallow berms on either side; incision depths range from 2.5-15 m, widths are 90-360 m, and

124   berm heights are typically 1-3 m (Figure 2c). The orientation of these scours is typically E-W or SE-NW (average orientation

125   is 0.94°) and is thus consistent with iceberg transport from the Pine Island and Thwaites glacier fronts with the coastal current.

126   However, the cross sections of some scours can change direction and vary along their length from a single v-shaped to wider

127   u- or w-shaped, the latter indicating that the geometry of the iceberg base has varied as the iceberg was dragged through the

128   sediment (consistent with either keel break-off or iceberg rotation). Some scours also terminate abruptly in rounded

129   depressions, encircled by a shallow berm. Such iceberg grounding pits or iceberg plough ridges indicate where seafloor

130   scouring terminated (e.g., Jakobsson et al., 2011). Most often there are no other incisions on the seafloor that cross-cut the

131   plough ridges, suggesting that the icebergs either lifted-off from the seafloor once enough melting had occurred or perhaps

132   toppled (rotated vertically due to an unstable height:width ratio; e.g., Bass, 1980 and Ruffman, 2005) allowing them to float

133   away freely without incising the seafloor further.

134   Detailed inspection of the scours reveals that some have either sinuous edges over length scales of a few hundred

135   metres, variable depths along the centre of the scour, again at length scales of hundreds of metres, or exhibit both morphologies

136   together. We interpret this variability as being formed by icebergs that have ploughed the seafloor and "wobbled", either from

137   side to side or are close to flotation and have bobbed up and down on the seafloor under the influence of tides, currents and/or

138   winds, or a combination of these factors (cf. Barnes and Lien, 1988; Lien et al., 1989). A particularly intriguing seafloor

139   morphology of crossed u-shaped scours that appear to be linked together are observed on the southern part of Bear Ridge in

140   water depths of ~275 m (Figure 2a). We suggest that these scours were formed by flat-bottomed icebergs that incised the

141   seafloor as they were transported on to a shallower part of the ridge, where they halted. Then, under the influence of local

142   currents, winds or tides, the bergs were dragged through the sediment in a perpendicular direction to their original pathway.

143   Alternatively, two different icebergs may have ploughed scours perpendicular to each other, thus generating a crossed shape.

144   Like the iceberg plough ridges, these scours have sharply defined and uninterrupted edges and berms suggesting that when the

145   icebergs did eventually move off the seafloor it was due to melting or toppling and no further marks on the seafloor were made.

146

147   **Table 1: Bear Ridge iceberg scour metrics**

Av. depth (m)	Depth range (m)	Av. width (m)	Width range (m)	Av. orientation
7	2.5-14	189	90-357	0.94°

148
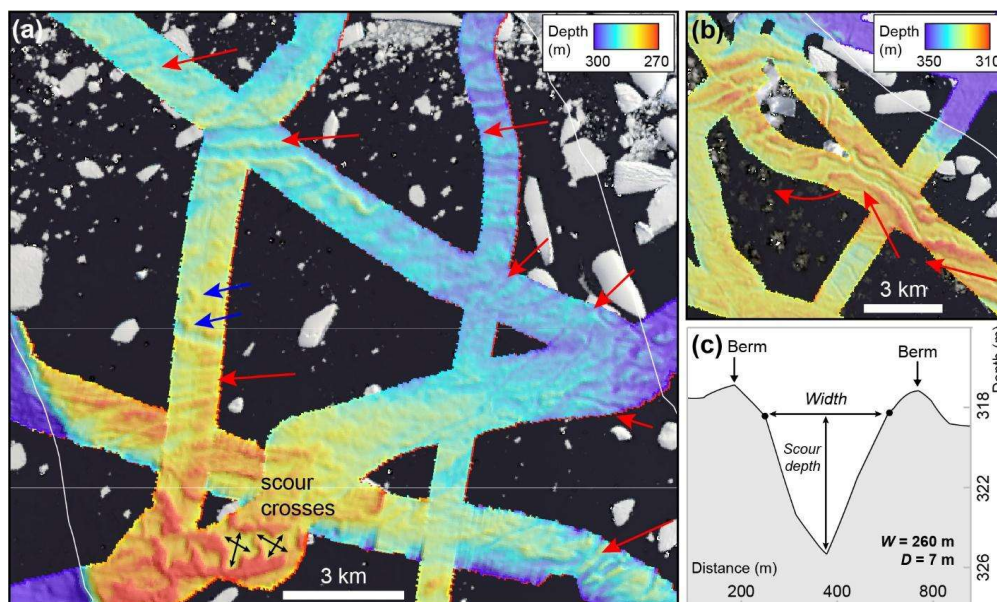
Figure 2: Examples of iceberg scour types from Bear Ridge (boxes a and b located as shown on the map in Figure 1). The red arrows show likely iceberg transport paths westwards from the eastern Amundsen Sea and across Bear Ridge; blue arrows show iceberg plough ridges (berms); black arrows show the perpendicular direction of iceberg scouring in the crossed forms. Panel c) presents a schematic of a typical scour cross-section found on Bear Ridge.

2.2 Sediment density and shear strength

To assess the influence of sediment resistance on iceberg grounding, we compiled wet bulk density (WBD) and shear strength data for representative sediment cores recovered from the Amundsen Sea (Figure 3; Smith et al., 2011; Clark et al., 2024). Whole core WBD was determined using a GEOTEK multi-sensor core logger following standard methods (Niessen et al., 2007) while shear strength was measured with a shear vane (Smith et al., 2011; Clark et al., 2024).

The composition of seafloor (<15 m) sediments in the Amundsen Sea is variable, but typically consists of three broad lithological units. The uppermost unit, directly at the seafloor, consists of soft, water-rich muds with variable biogenic content. These sediments were deposited in an open or seasonally sea-ice covered glaciomarine environment distal (>25 km) from the ice sheet grounding line (Smith and Hogan, 2024) and are characterised by low shear strength and density values (<5 kPa, ~1.4-1.6 × 10^3 kg/m^3). Beneath these sediments, coarser-grained stratified to structureless, sandy to gravelly, terrigenous sediments occur. These 'transitional' sediments were deposited at or close to (<25 km) to the ice sheet grounding line and lie directly above subglacial sediments below. The subglacial sediments in the basal unit consist of stiffer/denser, and largely structureless diamictons deposited subglacially during the Last Glacial Maximum, either as deformation till (>5-25 kPa, 1.8-2.2 × 10^3 kg/m^3) or 'stiff' compacted tills (>50 kPa, >2.0 × 10^3 kg/m^3). Thicknesses of each unit vary, but postglacial glaciomarine muds tend to be thicker on the inner shelf, particularly where sedimentation is focussed in bathymetric troughs/depressions. Conversely, on shallow banks such as Bear Ridge or former pinning points (see Hogan et al., 2021), these softer muds tend to be much thinner (<1m), so that stiffer sediments and (crystalline) bedrock occur much closer to the seafloor. Figure 3 presents samples from all of the three units characterized by different wet bulk density and shear strength.

Compared to other sectors of the Amundsen Sea, comparatively few sediment cores have been recovered from Bear Ridge due to a combination of perennial sea-ice cover, and a general scientific focus on the glacial troughs. The seafloor drill rig MARUM-MeBo70 was used at three locations on the western flank of Bear Ridge (Gohl et al., 2017), revealing that

175   indurated mudstones, likely of Eocene-Miocene age, crop out very close to the seafloor. Shear strength was not measured but

176   density values range from 1.5-1.9 $\times 10^3$ kg/m³. One 2.7 m gravity core recovered from glacial lineations on the top of Bear

177   Ridge has density values ~1.3-2.1 $\times 10^3$ kg/m³, which are comparable to other glaciomarine/deformation till sequences

178   recovered elsewhere in the Amundsen Sea (Figure 3). Crucially, all of the three sedimentary strata described above overlie a

179   solid crystalline basement and/or lithified sedimentary strata that cannot be penetrated by iceberg ploughing.

180
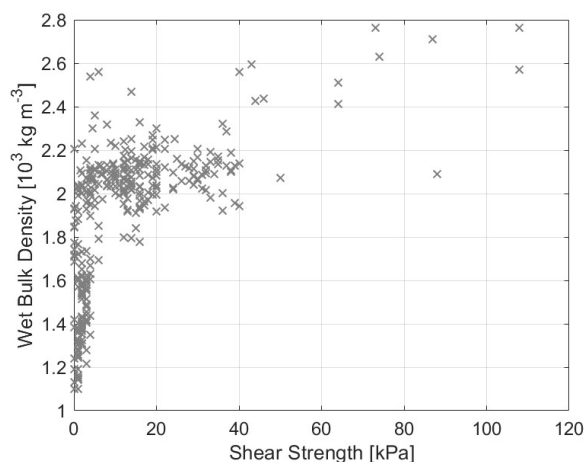
181

182   **Figure 3: Observed sediment properties for selected cores from the Amundsen Sea that span three layers: the uppermost soft, water-**
183   **rich muds; coarser-grained stratified to structureless, sandy to gravelly, terrigenous transitional sediments; stiffer and/or denser**
184   **subglacial diamictons.**

185   **3 Modelling iceberg dynamics and grounding**

186   In order to improve the simulation of iceberg drift, grounding, and ungrounding, we build up a theoretical framework that

187   defines the relevant forces at play. We consider drivers of iceberg motion – such as surface winds and ocean pressure gradients

188   – as well as forces that dissipate mechanical energy via the effects of bottom sediment resistance and solid bedrock friction.

189   **3.1 Forces acting on freely floating icebergs and their representation in NEMO**

190   Floating icebergs are driven by the combined effect of relative winds (on the iceberg's upper surface and sides of the iceberg

191   freeboard), sea-ice drag, ocean waves, and ocean pressure gradients and relative ocean currents integrated over the depth of

192   the submerged keel and along the iceberg's basal surface (Merino et al., 2016). Icebergs are also subject to the Coriolis force

193   (Marsh et al., 2015; Cenedese and Straneo, 2022). The effect of tides (if represented) is indirect: tides alter the sea surface

194   height gradients, and hence, the water column thickness, ocean pressure gradients, and ocean drag. The acceleration of a freely-

195   floating iceberg as it moves (Bigg et al, 1996; Condron and Hill, 2021; Marsh et al., 2018) can be expressed as:

196    $$\frac{d\vec{u}}{dt} = \vec{a}_{pressure\ gradient} + \vec{a}_{Coriolis} + \vec{a}_{ocean\ drag} + \vec{a}_{atmos.\ drag} + \vec{a}_{sea-ice\ drag} + \vec{a}_{waves} \qquad (1)$$

197   where terms on the right-hand side denote accelerations due to the ocean pressure gradient, the Coriolis force, ocean drag,

198   atmospheric drag on icebergs, sea-ice drag, and wave drag (see the supplementary Table D1 for a list of all symbols used).

199   Importantly, grounded icebergs are also decelerated by an additional term, $\vec{a}_{ground}$, which represents the sum of all dissipative

200   forces acting on an iceberg. Notice the qualitative analogy between the above budget and the material derivative of water

201   parcels in the ocean. One important difference compared to fluid parcels is that the iceberg acceleration budget does not include

202   a $\vec{u} \cdot \nabla \vec{u}$ term. We assume that there is no continuous field of interacting icebergs, and so $\nabla \vec{u} = 0$ because icebergs are treated

203   as isolated rigid, solid bodies (in NEMO they are in fact represented as moving point particles when it comes to advection).

204   The direct acceleration that the atmosphere, ocean and sea-ice flows impose on icebergs can be understood in

205 terms of the turbulent drag that the fluid exerts on the berg. This turbulent drag is assumed to be a quadratic function of the

206 speed of the iceberg relative to the fluid:

207 $\vec{a}_{drag} = -C_{drag}|\vec{u} - \vec{u}_{fluid}|(\vec{u} - \vec{u}_{fluid})$ (2)

208 where C_{drag} represents an effective drag coefficient that is different for air, seawater and sea-ice, and has units of an inverse

209 length scale related to the horizontal extent of the iceberg (Martin and Adcroft, 2010). The effective drag coefficient takes into

210 account the efficiency of momentum transfer between the fluid and the iceberg, the density ratio between the fluid and the

211 iceberg, and the iceberg area exposed to the drag. The typical order of magnitude of this parameter when applied to ocean—

212 iceberg drag is 10^{-4} $[m^{-1}]$ for thick tabular icebergs in the Amundsen Sea. Analogously to a turbulent drag, the sea-ice pack

213 also exerts a drag on icebergs, especially in regions with a high sea-ice concentration (Marson et al., 2024). While the quadratic

214 formulation of equation (2) is well established for high Reynolds numbers in the ocean and atmosphere, its application to sea-

215 ice is used for simplicity, but little is known about its validity.

216   When considering ocean drag, it is important to account for the vertical shear in the upper ocean, which can

217 significantly impact iceberg motion (FitzMaurice et al., 2016). The existing NEMO algorithms use the depth-averaged ocean

218 velocity to estimate the ocean drag term:

219 $Old \ \vec{a}_{ocean \ drag} = \frac{C_{drag}}{D_{keel}} \left|\vec{u} - \int_{D_{keel}}^{0} \vec{u}_{ocean}(z) \, dz\right| \left(\vec{u} - \int_{D_{keel}}^{0} \vec{u}_{ocean}(z) \, dz\right),$ (3)

220 but the nonlinearity of the drag formulation means that equation (3) is inaccurate. In the update that we propose here, we

221 consider the ocean currents at each depth level and average the resulting drag over the iceberg keel depth to arrive at an

222 improved representation of ocean drag:

223 $\vec{a}_{ocean \ drag} = \frac{C_{drag}}{D_{keel}} \int_{D_{keel}}^{0} |\vec{u} - \vec{u}_{ocean}(z)|(\vec{u} - \vec{u}_{ocean}(z)) \, dz,$ (4)

224 where D_{keel} is the keel depth.

225   Another significant source of acceleration for icebergs is the horizontal gradient in ocean pressure at different depth

226 levels. Gradients in sea-surface height (SSH) form a large component of the horizontal pressure gradients, but density

227 variations also modify pressure gradients within the water column. This latter effect was not represented in the existing iceberg

228 dynamics in NEMO, and is introduced here. For example, in the x-direction, at each depth level z, we have a pressure gradient

229 component:

230 $\frac{\partial\left(\frac{P(z)}{\rho_0}\right)}{\partial x} = gh(z)\frac{\partial\left(\frac{\langle\rho'(z)\rangle}{\rho_0}\right)}{\partial x} + g\left(\frac{\langle\rho'(z)\rangle}{\rho_0}\right)\frac{\partial h(z)}{\partial x} + g\frac{\partial h(z)}{\partial x}$,   (5)

231 where $\langle\rho'(z)\rangle = \frac{1}{z}\int_{0}^{z}(\rho(z) - \rho_0)dz'$ is the density anomaly, relative to the reference Boussinesq density ρ_0, averaged over

232 the overlying water column, g is the magnitude of the acceleration due to gravity, and $h(z)$ is the water-column thickness

233 above level z. Under the Boussinesq approximation, the contribution of the second term on the RHS may be neglected. In

234 addition to large-scale dynamical features, tides also contribute to SSH gradients, while SSH anomalies are considered a major

235 driver of iceberg motion, especially for weakly-grounded icebergs (Brown et al., 2017).

236   In addition to drag and pressure forces, icebergs furthermore respond to the Coriolis force due to the planetary rotation,

237 which gives rise to an acceleration at a right angle relative to the velocity vector:

238 $\vec{a}_{Coriolis} = -f\hat{k} \times \vec{u}$,   (6)

239 where f is the Coriolis parameter.

240 **3.2 Sediment resistance**

241 Grounded icebergs are subject to additional sources of acceleration and deceleration such as sediment resistance and solid-

242 body friction, which have so far not been represented in the NEMO iceberg module and are introduced here for the first time.

243 Here we make a distinction between several different cases: icebergs that plough only into the sediment and remain in motion

244   or halt; icebergs whose base reaches the solid basement but remain in motion; and icebergs whose motion comes to a stop

245   when grounded in the sediment and/or on the basement. Here we first describe the resistance experienced by a moving berg

246   ploughing through sediment.

247   There is a specialized body of literature discussing the interaction of icebergs with seafloor sediments. Empirical

248   observations and theoretical considerations suggest that sediment resistance can be decomposed into three different

249   mechanisms. An iceberg ploughing into sediments creates a wedge of sediment, composed of fracture plates (Chari et al.,

250   1975; Chari et al., 1980). The weight of this wedge pushes back on the part of the iceberg's frontal face that has ploughed into

251   the sediment with a force (in units of N):

252    $\frac{\gamma'(H+D)^2 W}{2} \approx \frac{\gamma' D^2 W}{2}$ (7)

253   where γ' is the submerged unit weight of the bottom sediment (in units of N m^{-3}), W is the width of the scour, D is the depth

254   of the scour, and $H \ll D$ is the height of the excavated sediment above the level of the surrounding seafloor (Chari et al., 1975;

255   Chari et al., 1980). The submerged unit weight γ' [N m^{-3}] in turn can be expressed as a function of the saturated sediment

256   density ρ_{sat} [kg/m^3] and the density of water ρ_{water} [kg/m^3]:

257    $\gamma' = g(\rho_{sat} - \rho_{water})$.   (8)

258   Furthermore, there are shear stresses acting along the surfaces of the fracture plates within the wedge of sediment

259   excavated by the iceberg:

260    $2\tau DW$ (9)

261   where τ is the shear strength of the sediments in units of Pa (Chari, 1975; Chari et al., 1980). Lastly, as the excavated wedge

262   is pushed forward along the path of the iceberg scour, the sides of the wedge experience lateral friction against the undisturbed

263   surrounding sediments:

264    $\frac{\sqrt{2}}{2}\tau D^2$.   (10)

265   This gives rise to a three-term expression for the maximum possible sediment resistance, which acts in the direction

266   opposite to the iceberg drift if it is in motion, or opposite to the net driving force if the iceberg is static:

267    $\vec{a}_{sediment\ max} = \begin{cases} -\left[\frac{\gamma' D^2 W}{2} + 2\tau DW + \frac{\sqrt{2}}{2}\tau D^2\right]\hat{u}/M_{iceberg}\ , & |\vec{u_0}| > 0 \\ -\left[\frac{\gamma' D^2 W}{2} + 2\tau DW + \frac{\sqrt{2}}{2}\tau D^2\right]\hat{a}_{net\ drivers}/M_{iceberg}\ , & |\vec{u_0}| = 0 \end{cases}$ (11)

268   where $M_{iceberg}$ is the iceberg mass, $\hat{a}_{net\ drivers}$ indicates a unit vector in the direction of the net driving force (the sum of all

269   nondissipative forces that drive iceberg motion) , $\hat{u}$ indicates a unit vector along the **projected** direction of future motion, which

270   depends both on the present velocity and on the net driving force (see below), and $\vec{u_0}$ is the present velocity of the iceberg. In

271   the model implementation (Section 3.4), the sediment resistance is not allowed to drive a net acceleration but only to decelerate

272   iceberg motion or to oppose the forces trying to set an iceberg in motion, hence why the above is formulated as a maximum

273   force.

274   Sediment thicknesses in different polar regions, and hence the maximum scour depth, differ markedly between areas

275   of glacially eroded (crystalline) bedrock that are completely stripped of sediment and thick sequences of more deformable

276   glaciomarine muds and subglacial tills. The latter can be 10s to 100s of meters thick, particularly in bathymetric depressions

277   such as glacial troughs. Following our Amundsen Sea example, the observed scours (Section 2.1) and compiled sediment

278   properties (Section 2.2) inform our decision to assume the existence of a uniform 8-m sediment layer with a wet bulk density

279   of 1.8×10^3 kg/m^3 and shear strength of 6 kPa. Beneath this single uniform sediment layer we assume the existence of a

280   basement. Thus, iceberg ploughing is allowed to occur up to a maximum of 8-m depth while it remains in motion, but then

281   other forces come into play, described next.

3.3 Gravity, solid-body friction, and static friction

When a moving grounded iceberg ploughs through all the sediment and reaches a sloping basement, it can move up the basement slope if the berg has enough momentum and/or sufficient sources of sustained acceleration (Chari 1975). As the berg moves up the slope, it is lifted upwards, its freeboard increases, and as a result, the buoyancy force of the ocean no longer balances the weight of the iceberg and a force directed into the basement supports the remainder (Figure 4). This gives rise to a gravitational force, which converts the kinetic energy of the iceberg motion into potential energy upon grounding, and also causes a solid body friction between the berg and the basement.
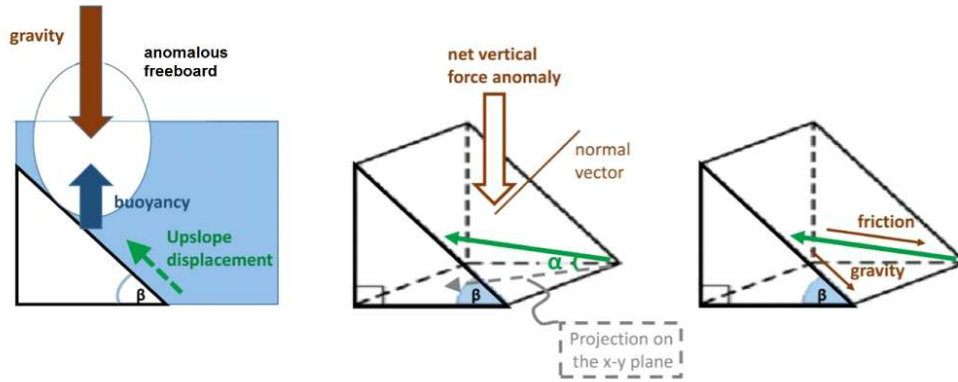
Figure 4: Vertical force budget. An idealized schematic of an iceberg trajectory (green arrow) going up a topographic slope. The angle of the trajectory (solid green arrow) relative to its projection on the horizontal x-y plane (dashed grey arrow) is denoted α. The local maximum slope of the topography is denoted β. The vector normal to the topography is indicated with a brown line. Schematic angles not shown to scale with respect to the relevant topographic slopes.

Lifting the iceberg out of floatation means that a portion of the iceberg's weight is no longer supported by the buoyancy of ice relative to seawater. The vertical displacement yields a deficit of $\rho_{water} H_{freeboard\,anom.}$ in the mass of seawater displaced by the berg per unit area, and a corresponding net downwards gravitational force. Dividing this force by the berg mass per unit area, we arrive at an acceleration

$$\frac{\rho_{water}}{\rho_{ice}} \frac{H_{freeboard\,anom.}}{H_{Total}} \vec{g} \; . \tag{12}$$

where the above takes into account the density difference between the iceberg $\rho_{ice} = 875$ kg/m^3 (including firn air trapped in the ice) and the ambient sea water $\rho_{water} = 1025$ kg/m^3, and $\vec{g}$ is the gravitational acceleration vector.

This new force has a projection down the sloping topography:

$$\frac{\rho_{water}}{\rho_{ice}} \frac{H_{freeboard\,anom.}}{H_{Total}} g \sin\beta \; . \tag{13}$$

where the topography has a local maximum slope β (Figure 4). It is the horizontal components of the force balance that are of interest here. We can furthermore express the projection of the gravitational force directed straight down the slope as a horizontal acceleration term:

$$\vec{a}_{gravity} = \frac{\rho_{water}}{\rho_{ice}} \frac{H_{freeboard\,anom.}}{H_{Total}} g\,(\sin\beta\cos\beta)\hat{s} \tag{14}$$

where $\hat{s}$ is a unit vector in the x-y horizontal plane aligned with the direction of the maximum topographic slope at the location of the iceberg.

There is another gap in the literature when it comes to the solid-body friction between the base of the iceberg and the basement beneath any sediments. One may, however, draw a qualitative analogy to the friction between glaciers and rock, whose representation in models can also be reduced to a solid-body (Coulomb type) sliding law (Fowler et al., 2010), which is independent of the speed in certain regimes. This term in the force balance is briefly discussed in Chari's dissertation (Chari,

313   1975). Generally, Coulomb friction is assumed to be proportional to the normal confining force at the interface between the

314   two solid objects, in our case the seafloor basement and the base of the iceberg. When the iceberg is in contact with basement,

315   this normal force is a projection of the net vertical imbalance between gravity and buoyancy from equation 12:

316    $\frac{\rho_{water}}{\rho_{ice}} \frac{H_{freeboard\ anom.}}{H_{Total}} g \cos\beta$,   (15)

317   where g is the magnitude of the gravitational acceleration. If an iceberg moves up a slope at an angle α relative to the horizontal

318   plane, the magnitude of the Coulomb friction in the sloping plane can be expressed as

319    $\frac{\rho_{water}}{\rho_{ice}} \frac{H_{freeboard\ anom.}}{H_{Total}} g\ \mu \cos\beta\ \cos\alpha$ (16)

320   where μ is a dimensionless coefficient of solid body friction, whose value for the interaction between icebergs and the seafloor

321   basement is not known. Equation (16) describes a deceleration term acting against the horizontal direction $\hat{u}$ of motion (Figure

322   4) of moving icebergs. The derivation of equation (16) is analogous to the derivation of (14) except that this time we do not

323   project the net vertical disequilibrium force along the topographic slope but along the direction of the iceberg's trajectory,

324   which is oriented at an angle α relative to the horizontal plane (Figure 4). The kinetic friction has a vector orientation opposing

325   the iceberg velocity:

326    $\vec{a}_{solid} = -\frac{\rho_{water}}{\rho_{ice}} \frac{H_{freeboard\ anom.}}{H_{Total}} g\ \mu \cos\beta\ \cos\alpha\ \hat{u}$.   (17)

327   In the model implementation (Section 3.4), the magnitude of the kinetic friction vector $\vec{a}_{solid}$ is limited, so that it never drives

328   a net acceleration. The value of the non-dimensional coefficient μ cannot be constrained directly and could only be inferred

329   from the resulting iceberg grounding behaviour. In this study, we test a range of values but use $\mu = 0.002$ in simulations with

330   a realistic Amundsen Sea model configuration (See Appendix B).

331   We note that the coefficient of Coulomb friction μ is usually assumed to be different in the case of moving objects

332   (kinetic friction) versus objects at rest (static friction, μ_{stat}). Usually, the coefficient of static friction μ_{stat} is greater than or

333   equal to the value of the kinetic friction coefficient for the same type of surfaces under similar conditions. Another noteworthy

334   difference between the kinetic and static solid body friction is related to the orientation of the frictional force vector. In the

335   case of static friction, there is no motion, so friction does not act in a direction opposite to the velocity vector, which is zero.

336   Instead, static Coulomb friction and sediment resistance jointly act in a direction opposing the net sum of all acceleration terms

337   that try to set an object into motion. Therefore, in the case of grounded icebergs, the maximum possible deceleration due to

338   static friction is:

339    $\vec{a}_{static-soli} = -\frac{\rho_{water}}{\rho_{ice}} \frac{H_{freeboard\ anom.}}{H_{Total}} g\mu_{stat} \cos\beta\ \cos\alpha\ \widehat{a_{net}}$ (18)

340   which is similar to the expression for kinetic friction, but here, were orient the vector against the sign of the net acceleration

341    $\vec{a}_{net\ drivers}$, which includes fluid and ice drag, the Coriolis, and gravitational accelerations but none of the dissipative

342   accelerations, and is aligned with the unit vector $\widehat{a_{net}}$. In our study we impose a static coefficient μ_{stat} that is 100 times larger

343   than the corresponding kinetic coefficient μ, which is an arbitrary choice tested below.

344   Last but not least, an iceberg moving along solid-basement topography with non-constant slopes experiences changes

345   in motion due to the surface geometry. For example, if an iceberg moves up a steeper slope, some of its horizontal momentum

346   is reoriented in the vertical direction. This gives rise to an apparent horizontal deceleration term that is independent of gravity

347   and buoyancy, unrelated to turbulent drag, and unrelated to dissipative forces such as sediment resistance or solid body friction.

348   For example, if the topographic slope β changes at a rate $\partial\beta/\partial x$ along the pathway of a grounded iceberg moving in the x-

349   direction, then u, the x-component of the iceberg's horizontal velocity also changes as:

350    $\vec{a}_{cuvature} \cdot \hat{x} = -|u^2 \tan\beta\ |\frac{\partial\beta}{\partial x}\hat{x}$ (19)

351   and analogously for a component $\vec{a}_{cuvature} \cdot \hat{y}$ along the y-direction. The term $\vec{a}_{cuvature}$ represents the direct impact of

352   seafloor basement geometry on horizontal velocity and can be understood through dimensional analysis. For example, in

353   equation (19), the factor u^2 has dimensions of length squared over time squared $\left[\frac{L^2}{T^2}\right]$, while the horizontal spatial derivative

354     $\frac{\partial}{\partial x}$ has dimensions of inverse length $[L^{-1}]$. Therefore, $\vec{a}_{cuvature}$ is an acceleration term with dimensions of length over squared

355   time $\left[\frac{L}{T^2}\right]$. Qualitatively, the tangent $tan\,\beta$ of the topographic slope β tells us how changes in the slope along the horizontal

356   direction re-orient the velocity vector along the vertical direction. For instance, when the slope gets steeper, the iceberg's

357   velocity vector is deflected more towards the vertical direction. Numerical tests demonstrate that the term $\vec{a}_{cuvature}$ becomes

358   non-negligible compared to other acceleration terms when icebergs slide along realistic topography. However, this happens

359   only when the angle of the interpolated topography changes along the iceberg's pathway. The curvature factor is non-negligible

360   if we focus on the small-scale shape and evolution of iceberg bottom scours, but does not play a first-order role in the overall

361   residence times of grounded icebergs on the scale of the ocean domain resolution as revealed by the tests in Section 4.

362   In total, then, the new iceberg grounding model is made up of 4 terms, each of which applies under different

363   conditions:

364     $\vec{a}_{ground} = \vec{a}_{sediment} + \vec{a}_{gravity} + \vec{a}_{solid} + \vec{a}_{curvature}\,,$ (20)

365   and when an iceberg is grounded the above terms (if present) are added to the full iceberg momentum budget.

366

3.4 Implementation of the new iceberg algorithms in NEMO

368   We implement the relevant iceberg dynamics and grounding theory as an update (Kostov et al., 2025b) to the existing

369   representation of icebergs in NEMO. The iceberg model in NEMO operates within the ocean domain. However, iceberg motion

370   is not confined to the resolved ocean grid, and instead bergs are dynamically represented as Lagrangian mass particles that

371   propagate across and within ocean grid cells. For the purposes of calculating melt rates, as well as turbulent drag, each iceberg

372   is associated with horizontal and vertical dimensions: length, width, and thickness. The iceberg motion is calculated using a

373   4th-order Runge-Kutta scheme (Marsh et al., 2015; Merino et al., 2016). Acceleration, velocity, local SSH slope, and horizontal

374   position are calculated at each stage of the Runge-Kutta scheme and the final estimate for a given iceberg timestep is a weighted

375   sum of the result from each of the four Runge-Kutta stages.

376   As the icebergs move within the resolved grid cells, ocean properties such as velocity, temperature, SSH, and

377   bathymetry are horizontally interpolated onto the sub-gridscale position of the bergs. We calculate vertically-averaged ocean

378   drag terms that we update and apply as acceleration terms within each stage of the Runge-Kutta scheme for iceberg dynamics.

379   At each Runge-Kutta stage, we also apply horizontal pressure gradients interpolated onto iceberg positions. The pre-existing

380   code included only the gradient components due to SSH anomalies. Here we also account for the pressure gradient terms that

381   arise due to water density anomalies, exactly as they are calculated and applied in the dynamics of the liquid ocean domain.

382   Our calculation of the pressure gradient terms is therefore compatible with the multiple vertical coordinate systems that are

383   available in NEMO, e.g, fixed z-level or z*-coordinates that stretch and contract matching the SSH anomalies. In our

384   implementation, icebergs do not feel the component of the ocean pressure gradient due to the iceshelf load over iceshelf

385   cavities, as icebergs themselves cannot enter the cavities. However, icebergs are often found near the iceshelf edge even long

386   after they have calved. That is why, in algorithm, we mask the ice-shelves, such that icebergs in their vicinity can approach

387   the shelf edge without being exposed to unphysical pressure gradients.

388   The NEMO model has some existing, crude representations of iceberg grounding (Olivé Abelló et al., 2025). At each

389   of the four Runge-Kutta stages, these routines consider criteria under which iceberg velocity or components of the iceberg

390   velocity are set to zero as topographic obstacles are encountered. The grounding routines use the projected forward motion of

391   the iceberg and therefore have an implicit element. The pre-existing algorithms allow for two options: 1) icebergs come to a

392   complete stop when their keel reaches a topographic obstacle; or 2) the component of an iceberg's velocity vector normal to a

393   topographic obstacle is set to zero, while the tangential component is preserved.

394   In our new implementation, we also apply grounding routines at each stage in the Runge-Kutta scheme. However, we

395   represent the interaction between icebergs and the seafloor in terms of acceleration terms due to gravity, solid-body friction,

396   and sediment resistance (Section 4). These acceleration vectors are projected along the x and y-axes (zonal and meridional) of

397   iceberg motion, which are aligned with the ocean model grid (Figure 4). The acceleration/deceleration terms that we introduce

398   depend on the local slope of the topography and on the angle at which an iceberg moves relative to the horizontal plane (which

399   may be different from the maximum topographic gradient, Figure 4). In order to calculate these angles for each Lagrangian

400   iceberg particle, we track and store interpolated bottom topography along an iceberg trajectory and calculate the corresponding

401   slope angles.

402   In addition, we apply different solid-body friction coefficients depending on whether the grounded iceberg is in

403   motion or at rest. For numerical purposes, we do not set a zero speed as the threshold for assuming no motion. Instead, when

404   the speed drops below a small magnitude ($5 \times 10^{-5} \ m/s$), we set it to zero and assume a regime of static friction. This way

405   we avoid situations where we see numerical stick and slip of icebergs alternating between no motion and brief periods of very

406   slow motion.

407   Solid friction and 'sediment resistance' terms are also numerically peculiar in another way. While turbulent drag,

408   geometric deflection, and gravity can act in any direction to accelerate or decelerate a berg, the dissipative sediment resistance

409   and solid-body friction terms only act to decelerate motion. As described above, we do not allow the two dissipative terms,

410   solid friction and sediment resistance, to drive motion but only to bring an iceberg to a stop and/or keep it at rest. This

411   necessitates the use of a Boolean check that guarantees that either or both dissipative terms themselves do not give rise to

412   motion. Therefore, we impose that

413   $$\frac{d\vec{u}}{dt} = -\frac{\vec{u_0}}{\Delta t} \ \text{for} \ |\vec{a}_{solid} + \vec{a}_{sediment}| \geq \left|\vec{a}_{net \ drivers} + \frac{\vec{u_0}}{\Delta t}\right|, \tag{21}$$

414   where Δt is the model timestep and $\vec{a}_{net \ drivers}$ is the net sum of all acceleration terms that do not dissipate mechanical energy.

415   If the x- or y-component of velocity enters the case described in equation (21) at any of the four stages of the Runge-Kutta

416   solver, we raise a flag in our dynamics algorithm. The raised flag indicates that the calculated component of iceberg velocity

417   is zero. Even if the condition in (21) is achieved at only one of the four Runge-Kutta stages, the zeroing of the velocity

418   component is applied to the output of all four stages. Furthermore, if setting the x- or y-component of the velocity to zero

419   brings the total iceberg speed below $5 \times 10^{-5} \ m/s$, then we force the iceberg to stop.

420   The fact that iceberg motion is computed using a separate numerical scheme within the NEMO ocean domain allows

421   us to apply temporal substepping within the iceberg code while keeping the same time-step size for the ocean and sea-ice. We

422   thus define a parameter that sets the ratio of the ocean timestep to the shorter iceberg timestep. We find that allowing a shorter

423   iceberg timestep is numerically important when modelling the shape and evolution of iceberg scours because forces such as

424   gravity along the sloping topography may act on much shorter timescales compared to other sources of acceleration. (See

425   Appendix B, where the numerical relevance of sub-stepping is demonstrated in an idealized experiment with gravity but no

426   dissipative forces along a sloping bottom). At the same time, when modelling iceberg residence times and locations on the

427   resolved ocean grid, substepping becomes less critical (Appendix B).

428   **3.5 Amundsen Sea NEMO test cases**

429   We test our updated iceberg dynamics in a regional Amundsen Sea configuration of the Nucleus for European

430   Modelling of the Ocean (NEMO-v4.2.0, Madec et al. 2022). This includes the SI3 sea-ice component (Vancoppenolle et al.,

431   2023), a representation of ocean–ice-shelf interactions (Mathiot et al., 2017), and a Lagrangian iceberg module (Marsh et al.,

432   2015; Merino et al., 2016).

433   The extent of the regional domain, the horizontal resolutions (0.25°), and the topography are the same as in Caillet et
434   al. (2023), except that we do not impose a wall over Bear Ridge to block sea ice. We use 121 vertical levels as in Mathiot and
435   Jourdain (2023), with a thickness increasing from 1 m at the surface to 20–30 m between 100 and 1000 m depth. The cell
436   thicknesses are slightly compressed or stretched to follow the SSH variations (Z* coordinates), and cells adjacent to the sea
437   bed and ice shelf draft are described as partial steps (Adcroft et al., 1997).

438   The initial state and lateral boundary conditions are from 5-day mean outputs of the global simulation of Mathiot and
439   Jourdain (2023). Tides are neither generated nor prescribed at the boundaries, which is expected to have a limited impact in
440   the Amundsen Sea (Jourdain et al., 2019). Tides are relatively weak in the Amundsen Sea relative to other Antarctic sectors
441   (Jourdain et al, 2019). The surface boundary conditions are calculated through the bulk formula of Large and Yeager (2008)
442   from the JRA55-do atmospheric reanalysis (Tsujino et al., 2018).

443   We release icebergs in January of the first year of a simulation, i.e., 1979. Our aim with these simulations is to
444   demonstrate the new iceberg grounding physics. We are interested in a realistic historical setting, but in this study, we do not
445   aim to explore a broad range of long-term natural variability in the Amundsen Sea and its impact on icebergs. All the icebergs
446   in the Amundsen Sea simulations are released east of Bear Ridge and then allowed to drift, ground, and unground according
447   to the modelled ocean, atmosphere, sea ice and iceberg conditions. We conduct two sets of tests, each with a different iceberg
448   population. In the first set, labelled THICK hereafter, all test icebergs are tabular, with the same mass, 3.9×10^{11} kg, uniform
449   density of 875 kg/m^3, and thickness of 395 m. The density is based on realistic assumptions (Veldhuijsen et al., 2023) about
450   the firn air content of the ice shelves from which our hypothetical icebergs calve. This implies that our test icebergs have a
451   keel depth of approximately 337 m. In the second set of tests, labelled MEDIUM, all icebergs are 250 m thick, each with mass
452   of 3.8×10^{10} kg.

453   In this study we explore the results of two types of simulations, where each type of simulation is performed with each
454   type of iceberg thickness   . In the short simulations, labelled 'SHORT' hereafter, we initially seed a total of 497 identical
455   test icebergs one in each grid cell (~1/4° by ~1/4°) in the region east of Bear Ridge enclosed by 109.9° W, 106.2° W, 74.3°
456   S, and 72.0° S (Figure 1). While it is not realistic to expect hundreds of thick tabular icebergs to simultaneously occupy this
457   region, our icebergs do not interact with each other or block sea-ice (while sea-ice does impact icebergs). In our SHORT
458   simulations, even when icebergs melt, we do not allow any iceberg meltwater to be injected in the ocean, so as not to perturb
459   the background conditions with each set of 497 icebergs. We run this simulation with a large ensemble of icebergs but only
460   over the course of one full year spanning all seasons. Each of the grid boxes that we seed is a possible location where an
461   iceberg may be found, and hence, we explore the behaviour of thick tabular icebergs when exposed to the local conditions.
462   This large population allows us to analyze the statistics of iceberg dynamics while focusing specifically on the thick tabular
463   icebergs that are most likely to exhibit a long residence time when grounding on Bear Ridge. We aim to explore the differences
464   in the dynamical behaviour of icebergs of different sizes by comparing the THICK and MEDIUM populations. In order to
465   preserve the large thicknesses and horizontal areas in the THICK iceberg population, we do not allow the latter to melt during
466   a SHORT 1-year simulation.

467   We also run longer simulations labelled 'LONG', which are extended farther in time over 4 years to enable   a
468   comparison between modelled and observed iceberg scours. We seed a much smaller subset of 14 identical icebergs in a
469   narrower box, bounded by 109.9° W, 109.2° W, 73.9° S, and 73.5° S (Figure 1), on the eastern flank of Bear Ridge. We explore
470   the simulated scours left by the THICK icebergs whose motion is arrested on Bear Ridge. In simulation LONG, we do allow
471   THICK icebergs to melt, as that affects their motion and residence times along the bottom. This meltwater is injected in the
472   ocean and added to the precipitation at the surface.

4 Results: Force balance and behaviour of thick tabular icebergs in the Amundsen Sea configuration

In our Amundsen Sea numerical simulations, we observe the behaviour of thick tabular icebergs that are less typical of the Arctic but often found near Antarctica and whose large volume and mass plays an important role in their dynamics (Wagner et al., 2017). We are interested in the forces that act on these large icebergs in free flotation, upon grounding, and upon ungrounding. Although our main focus is the behaviour of grounded icebergs, we also aim to understand the forces acting on freely floating icebergs before they may ground and after they unground. In this analysis, we also test the impact of the new iceberg dynamics and grounding algorithms that we have implemented in NEMO in the important Amundsen Sea regional context.
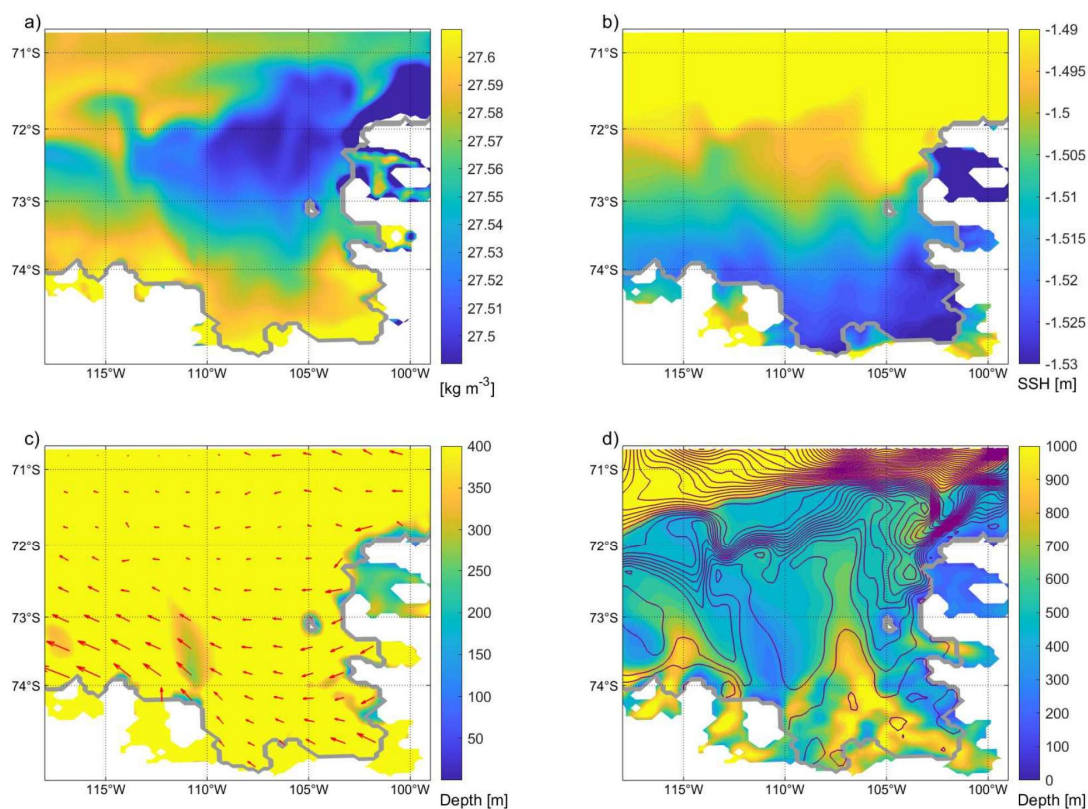
Figure 5: Climatology (1979 through 1982) of the Amundsen Sea configuration. a) potential density [kg/m³] referenced to the surface, vertically averaged over the top 310 m with shallower regions masked; b) sea-surface height [m]; c) wind stress vectors [N/m²]; d) barotropic streamfunction contours [0.1 Sv intervals]. The bottom depth [m] is superimposed in c and d. The depth range in c chosen to highlight the location of the shallow Bear Ridge and a wider depth range in d to highlight the alignment of streamlines and topography. The ice shelf edge is marked by the thick gray line.

489
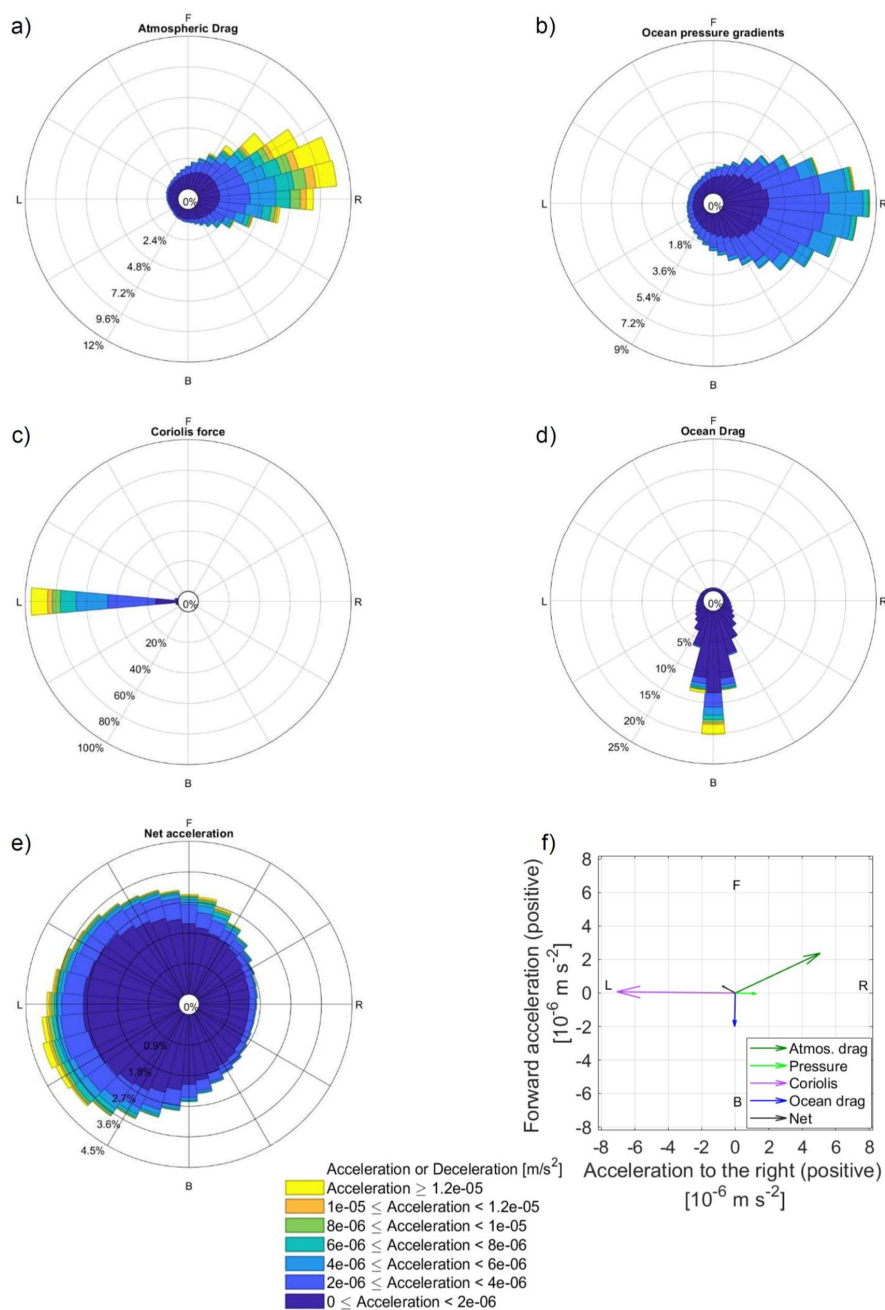
Figure 6: Contributions of atmospheric drag (a), the oceanic pressure gradients (b), the Coriolis force (c), the ocean drag (d), the net acceleration (e), and the average of a-d across all test icebergs and all timesteps (f) to the momentum budget of simulated freely floating THICK icebergs in the Amundsen Sea in the SHORT simulation. Directions are denoted as F (forward, along the iceberg's direction of motion), B (backward, against the direction of motion), L (to the left of the direction of motion), R (to the right). The full length of the radial bars indicates the probability density function of acceleration in a given direction. For each panel in a-e, the sum of all directions is 100%, but the bars along some of the directions are relatively smalls. For each bar in a-e, the range of acceleration magnitudes is indicated by the colours, and the probability of each magnitude class is indicated by the radial distance. Colour sections in a-e indicate the frequency distribution of the accelerations in each magnitude class. Note that the radial axis is different between panels a-e, while the colour scale is common to panels a-e. Panel f has a separate legend and a different colour scheme. The first 100 timesteps of the simulation, when the iceberg motion is initialized from rest, are omitted. Software written by Daniel Pereira was used to create the wind rose (https://www.mathworks.com/matlabcentral/fileexchange/47248-wind-rose, last access: November 2025, MATLAB Central File Exchange)

502

503

504
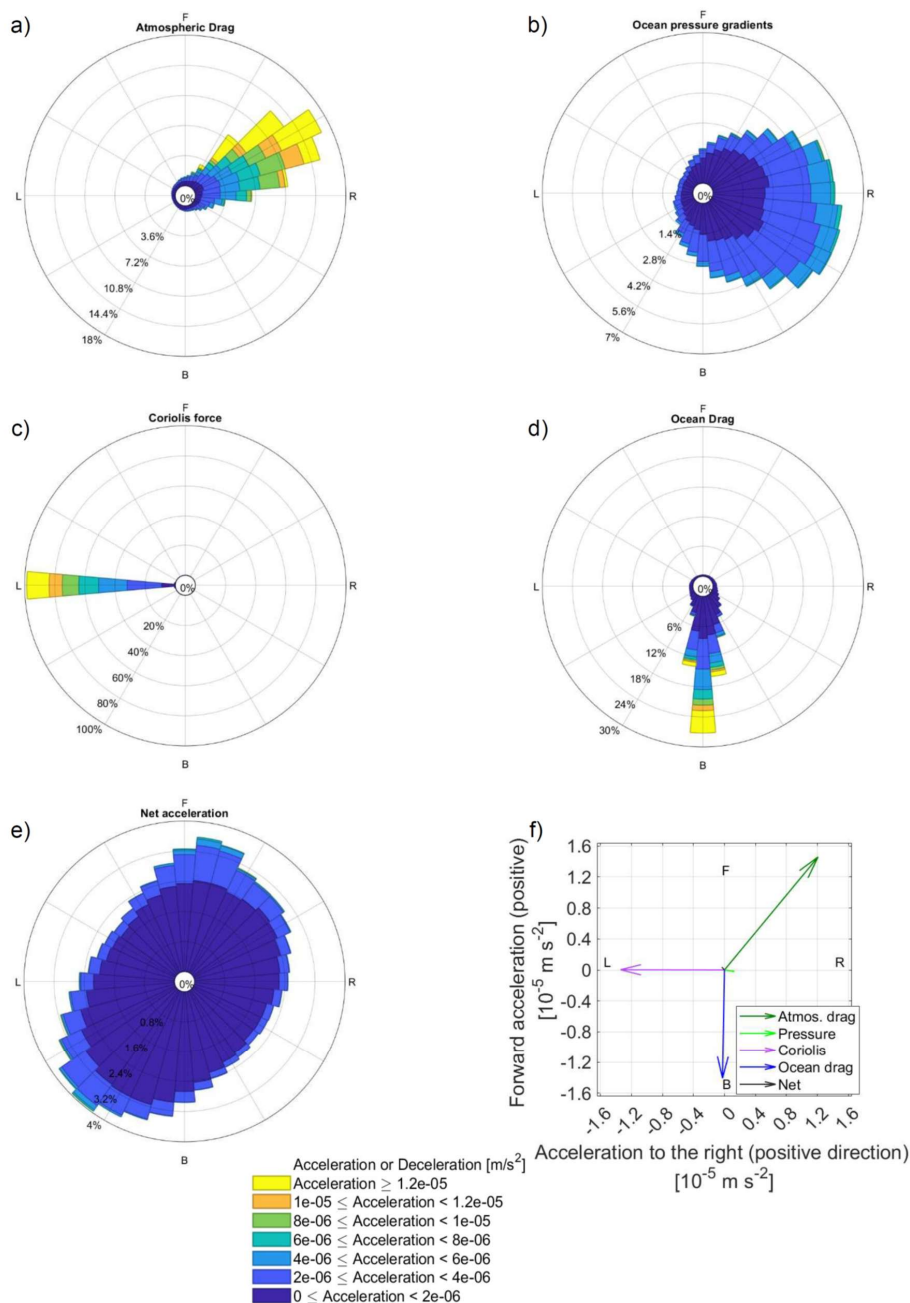
Figure 7: Same as Figure 6 but for freely floating MEDIUM icebergs in the Amundsen Sea in the SHORT simulation.

505

506

4.1 Background conditions and force balance of freely-floating icebergs

In order to understand the trajectories and behaviour of icebergs in the eastern Amundsen Sea, we first explore the wider climatic conditions, including the oceanic and atmospheric climatology and variability in the region. There is a relatively lower water column density to the east of the ridge compared to the water column over the ridge (Figure 5a), but this is compensated by a positive zonal SSH gradient between 112°W and 110°W (Figure 5b), which in combination with the Coriolis force would drive icebergs southward near the Ridge (Figure 5a). Overall, there is very little ocean transport across Bear Ridge although the prevailing winds are oriented north-westward across the ridge (Figure 5c,d).

Using model output from the large ensemble of freely-floating icebergs in Amundsen Sea Simulation SHORT, we compute statistics showing how often a given force acts along a particular direction relative to the iceberg motion (the length and orientation of the bars in the Figure 6 rose plots for THICK icebergs and Figure 7 for MEDIUM icebergs). We furthermore consider how often (the length of the individual color segments in Figures 6 and 7) a given force has a magnitude that falls within a particular range (the color scheme indicates the magnitude range). We point out that some forces represented in the iceberg model play a less prominent role compared to the main drivers. For example, the acceleration due to wave radiation is much smaller than 1.5×10^{-6} m s^{-2} and so is neglected from the figures, while the acceleration due to sea-ice drag is always smaller than the other terms (see Figure C1 in Appendix C).

We first consider the dynamics of freely-floating THICK icebergs in the period before they encounter the Bear Ridge or the shelf-edge, where they may ground or come to a stop. We also omit the first 100 timesteps of the simulation, when iceberg motion is initialized from rest. For freely-floating THICK icebergs, the most common situation by far is that the atmospheric drag, the Coriolis force acting on icebergs, and the ocean drag are nearly in a three-way balance (Figure 6) with very little net acceleration. The Coriolis force is oriented solely to the left, perpendicular to the direction of iceberg motion, while the acceleration due to wind stress and ocean pressure gradients is mostly oriented to the right of the direction of motion. On average, the corresponding forces on THICK icebergs are nearly orthogonal to the direction of motion and therefore do very little work on the freely floating large icebergs. This result is not peculiar to tabular icebergs in the Eastern Amundsen Sea but is more fundamental and agrees with the theoretical arguments of Wagner et al. (2017).

In our results, the (updated) ocean drag on freely floating icebergs plays a less prominent role compared to other forces and mostly opposes the forward motion of the bergs. Compare the small positive projection of the atmospheric drag along the forward direction of motion (Figure 6a and 7a) and the small deceleration due to ocean drag (Figure 6d and 7d). This result for large THICK icebergs may be expected on theoretical grounds. Here we briefly revisit the Wagner et al. (2017) arguments about the motion of large icebergs from a new perspective and with an attempt to recover the same result in fewer steps. We also specifically avoid making the assumption that the ocean's water column is in geostrophic balance. Unlike Wagner et al. (2017), we attempt to account for a realistic Ekman drift in our theoretical analysis and show that the same arguments remain valid.

We first consider the decomposition of the iceberg velocity $\vec{u}$ into a component that matches exactly the ocean's horizontal velocity $\vec{u}_{ocean}$ and a relative mismatch $\Delta \vec{u}$. The evolution, in an Eulerian sense, of the local ocean velocity over the upper ocean layer can be approximately expressed as:

$$\frac{\partial \vec{u}_{ocean}}{\partial t} \approx -f\hat{k} \times \vec{u}_{ocean} + \text{(Pressure gradient terms)} + \text{(Ekman ageostrophic acceleration due to wind stress)} \qquad (22)$$

where we have assumed that the main source of ageostrophic transport in the Ekman layer (of thickness δ) comes from the tendency for Ekman drift due to surface wind stress $\vec{\tau}_{atm-ocean}$. Under equilibrium conditions, the geostrophic component of $f\hat{k} \times \vec{u}_{ocean}$ balances the pressure gradient terms and the ageostrophic component of $f\hat{k} \times \vec{u}_{ocean}$ vertically averaged over the Ekman layer balances the wind-stress acceleration.

While the ocean water column contains an Ekman spiral, the icebergs do not, and this is a potential source of mismatch between the velocity of icebergs and the surrounding ocean. In our study, we focus on thick icebergs, whose keel depth exceeds

549 the depth of the Ekman layer. If we consider the relative iceberg-to-ocean velocity $\Delta\vec{u}$ averaged over the keel depth, we can

550 express the Ekman acceleration term vertically integrated over the Ekman layer and then averaged over the full keel depth of

551 the icebergs as

552 $$|\text{Ekman acceleration}| = \left|\frac{\tau_{atm-ocean}}{\rho_0 D_{keel}}\right| \text{ over the keel depth,} \tag{23}$$

553 such that the vertically-averaged Ekman component of $\vec{u}_{ocean}$ is $\frac{\tau_{atm-ocean}}{f\rho_0 D_{keel}}$. The Ekman acceleration averaged over the depth

554 of the Ekman layer is oriented along the wind direction such that the average Ekman drift $\frac{\tau_{atm-ocean}}{f\rho_0 D_{keel}}$ is to the left of the wind

555 direction in the Southern Hemisphere.

556 The ocean pressure gradients exert the same force on the submerged portion of the iceberg as they would on an

557 equivalent water parcel. Therefore, we can express the evolution of the iceberg-to-ocean velocity mismatch $\Delta\vec{u}$ as arising from

558 a set of ageostrophic and dissipative processes. We can ignore the small terms due to sea-ice drag and wave drag. Furthermore,

559 assuming that the horizontal gradients of $\vec{u}_{ocean}$ are small along the iceberg trajectory, we can focus on the Eulerian evolution

560 of $\Delta\vec{u}$:

561 $$\frac{\partial(\Delta\vec{u})}{\partial t} = \frac{\partial\vec{u}}{\partial t} - \frac{\partial\vec{u}_{ocean}}{\partial t} \approx$$

562 $$\approx -f\hat{k} \times \Delta\vec{u} - C_{drag-ocean}\Delta\vec{u}|\Delta\vec{u}| - C_{drag-atm}(\vec{u} - \vec{u}_{atmos})|\vec{u} - \vec{u}_{atmos}|$$

563 $$- \frac{\tau_{atm-ocean}}{\rho_0 D_{keel}} \tag{24}$$

564 Under the additional assumption that typically $|\vec{u}| \ll |\vec{u}_{atmos}|$, the above becomes

565 $$\frac{\partial(\Delta\vec{u})}{\partial t} \approx -f\hat{k} \times \Delta\vec{u} - C_{drag-ocean}\Delta\vec{u}|\Delta\vec{u}| + C_{drag-atm}\vec{u}_{atmos}|\vec{u}_{atmos}| - \frac{\tau_{atm-ocean}}{\rho_0 D_{keel}} \tag{25}$$

566 We assume that the main source of the mismatch $\Delta\vec{u}$, if present, can be attributed to the different atmospheric drag felt by

567 icebergs relative to the surrounding water column, which experiences Ekman drift. Notice that the first two RHS terms depend

568 on the relative iceberg-to-ocean velocity $\Delta\vec{u}$, while the last two terms depend primarily on winds. When winds input

569 momentum into iceberg motion, and into the surrounding water column, this creates a differential acceleration between the

570 iceberg and the ocean. If equation (25) is not in balance, the iceberg's relative speed $\Delta\vec{u}$ increases, and motion gets deflected

571 to the left by the Coriolis force until the first two terms on the RHS balance the last two, wind-dominated terms. In a steady

572 state, the Coriolis force and ice-ocean drag balance the wind-dominated last two terms in equation 25.

573 The question is whether the Coriolis term (the first on the RHS) is sufficiently large to balance the excess atmospheric

574 drag on icebergs (last two terms), or whether the atmospheric drag on icebergs and the Ekman acceleration on the water column

575 are balanced by a relative drag between the ocean and the iceberg (second RHS term). With $\tau_{atm-ocean}$ that is typically

576 $\sim 3 \times 10^{-1} Nm^{-2}$ in our simulated region of interest, for THICK icebergs, the Ekman acceleration is

577 $$|\text{Ekman acceleration}| = \left|\frac{\tau_{atm-ocean}}{\rho_0 D_{keel}}\right| \sim \frac{\sim 3 \times 10^{-1} Nm^{-2}}{(1025\,kg\,m^{-3})(\sim 350\,m)} \sim 10^{-8} \text{ to } 10^{-7}\,m\,s^{-2} \tag{26}$$

578 We point out that, following equation (2), both the acceleration due to wind drag and the acceleration due to ocean drag scale

579 proportionally to their corresponding effective drag coefficient C_{drag}. The latter has units of a characteristic inverse length

580 scale describing the iceberg $C_{drag} \propto 1/L_{iceberg}$ (see equation 2). In contrast, the Coriolis component of acceleration is not

581 proportional to the iceberg's characteristic lengthscale. Therefore, the ratios between the groups of acceleration terms are:

582

583

584

585

586

587 $\quad \dfrac{\left|C_{drag-atm}\vec{u}_{atmos}|\vec{u}_{atmos}|\right|}{\left|f\hat{k}\times\Delta\vec{u}\right|} \propto \dfrac{C_{drag-atm}|\vec{u}_{atmos}|^2}{f|\Delta\vec{u}|} \propto \dfrac{(|\vec{u}_{atmos}|^2)}{L_{iceberg}\,f|\Delta\vec{u}|}$

588 $\quad \dfrac{|Ekman\,|}{\left|f\hat{k}\times\Delta\vec{u}\,\right|} \propto \dfrac{\tau_{atm-ocean}}{\rho_0 D_{keel}f|\Delta\vec{u}|}$

589 $\quad \dfrac{|f\hat{k}\times\Delta\vec{u}\,|}{c_{drag-ocea}\,\Delta\vec{u}|\Delta\vec{u}|} \propto \dfrac{f/|\Delta\vec{u}|}{c_{drag-ocea}} \propto L_{iceberg}\,f/|\Delta\vec{u}|$ $\hspace{3cm}$ (27)

590 However, the effective coefficients for the atmospheric and oceanic drag on icebergs are dependent not only on the iceberg

591 dimensions ($\sim L_{iceberg}$), but are also proportional to the density of the respective ambient fluid: water or air. Hence, the

592 coefficient for ocean drag is much larger than the coefficient of atmospheric drag, while the characteristic lengthscales

593 $\frac{1}{c_{drag-ocean}} < \frac{1}{c_{drag-atm}}$. For example, in our LONG simulation with THICK icebergs, $\frac{1}{c_{drag-ocean}} \sim 10^4$ m, while the

594 atmospheric drag coefficient $\frac{1}{c_{drag-atm}}$ is on the order of 10^7 m, consistent with a 1:1000 density ratio between air and water.

595 In our region, the southeastern Amundsen Sea, $f \sim 1.4 \times 10^{-4} s^{-1}$, and the surface wind speed $|\vec{u}_{atmos}|$ is typically on the

596 order of $\sim 1\, to\, 10\, ms^{-1}$. Equation (27) then implies that if ocean drag were to match to the Coriolis force, the speed of

597 icebergs relative to the ambient currents would have to reach unrealistically high values $|\Delta\vec{u}| \sim \frac{|f|}{c_{drag-ocean}} \sim 1\, ms^{-1}$. On the

598 other hand, equation (27) implies that a relative iceberg-ocean speed

599 $|\Delta\vec{u}| \sim \frac{|\vec{u}_{atmos}|^2}{1000} \sim 1\, cm\, s^{-1}$ $\hspace{6cm}$ (28)

600 is enough for an appropriately oriented Coriolis force to balance the direct atmospheric drag on large tabular icebergs (order

601 $10^{-6}\, m\, s^{-2}$) and also the smaller but nonnegligible Ekman term (up to order $10^{-7}\, m\, s^{-2}$). Assuming that this balance holds,

602 the ocean drag that results from $\Delta\vec{u}$ can be estimated to be

603 $C_{drag-ocean}\Delta\vec{u}|\Delta\vec{u}| \sim 10^{-8}\, to\, 10^{-7}\, m\, s^{-2}$ $\hspace{5cm}$ (29)

604 consistent with our findings (Figure 6). This suggests that for large tabular icebergs, the fictitious Coriolis force is sufficient

605 *in magnitude* to balance the excess atmospheric drag while the relative iceberg-ocean drag remains small (Figure 6) in

606 agreement with our results for THICK icebergs. Notice that the iceberg-ocean drag is similar in magnitude to the impact of

607 Ekman drift. Therefore, we are able to recover the force balance of large THICK icebergs even in the presence of small but

608 nonnegligible Ekman flow.

609 $\qquad$ In addition, equation (27) explains the orientation of the force vectors needed to achieve balanced motion. Only the

610 Coriolis force is large enough to balance the excess atmospheric drag on icebergs relative to the water column. However, for

611 that to happen, the iceberg's motion relative to the ocean has to be oriented at 90° to the left of the atmospheric drag, so that

612 the Coriolis force can oppose the atmospheric drag. In this case, ocean drag would act against the direction of motion relative

613 to the ocean. In the case of freely-floating THICK icebergs, the icebergs' motion is on average at an angle of 63° relative to

614 the wind direction, which means that the Coriolis force balances almost 80% of the acceleration due to wind-stress (Figure 6f).

615 The remaining 20% are balanced by the relatively smaller ocean drag, which is indeed oriented against the direction of motion

616 (Figure 6f), as predicted on theoretical grounds.

617 $\qquad$ The Coriolis force forms part of the dominant balance and steers motion in a direction nearly perpendicular to the

618 driving force due to winds (Wagner et al., 2017). As a result, most of the time, the orthogonal wind stress force does not do

619 significant work along the pathway of motion of large tabular icebergs. The important Coriolis effect also projects onto a small

620 net acceleration to the left of the iceberg direction of motion (Figure 6), which differs from the Wagner et al. (2017) assumption

621 of zero net acceleration but still does very little work along the iceberg pathway.

622 $\qquad$ We can contrast the above results for THICK icebergs with our simulated MEDIUM icebergs, where the iceberg-

623 ocean relative speed and the associated ocean drag play a more prominent role (Compare Figure 7 for MEDIUM and 6 for

624 THICK icebergs). The ratio between ocean drag and the Coriolis force is 2/7 for THICK icebergs (Figure 6), while it is closer

625   to 1 for MEDIUM ones (Figure 7). At the onset of the SHORT simulations, the horizontal and vertical length scales of

626   MEDIUM icebergs are 2.6 and 1.6 times smaller, respectively, compared to THICK ones. Consistently, we see that $\frac{1}{C_{drag-atm}}$

627   at the beginning of the simulations is 2.5 times smaller for MEDIUM icebergs relative to the wider THICK ones. MEDIUM

628   icebergs experience further lateral and basal melting which causes additional reduction of their size relative to THICK icebergs.

629   Naturally, the Coriolis acceleration cannot change orientation and always remains directed to the left of the motion

630   even as the balance of forces is shifted. At the same time, for our MEDIUM icebergs, the atmospheric drag deviates from the

631   orthogonality to the iceberg trajectory and projects more strongly along the axis of motion (Figure 7). Thus, atmospheric drag

632   seems to drive a more pronounced forward motion for MEDIUM icebergs than for THICK ones. This in turn is matched by

633   the enhanced ocean drag deceleration.

634   Both for THICK and MEDIUM freely-floating icebergs, the pressure gradient force is oriented mostly to the right of

635   the direction of motion, but with larger and more noticeable deviations for MEDIUM icebergs (Compare Figure 6 and Figure

636   7). We can invoke a different line of reasoning to explain the orientation of the pressure gradient force. We expect on the

637   aforementioned theoretical grounds (equations 28 and 29) that THICK large tabular floating icebergs move with velocities

638   close to the ambient ocean currents (see also Wagner et al., 2017) in terms of both magnitude and direction. In our study, this

639   notion is confirmed by the smaller ocean drag (Figure 6d), which suggests a small relative velocity between icebergs and the

640   ambient water. This implies that the relationship between ocean pressure gradients and iceberg motion reflects the underlying

641   relationship between ocean flow and pressure gradients. The consistent orientation of the ocean pressure gradient force nearly

642   orthogonal to the direction of motion of THICK tabular icebergs (interpret Figure 6b) can be interpreted as an indication that

643   geostrophic transport is a major component of the ambient ocean flow in the region of our simulated icebergs, when vertically

644   averaging over the THICK keel depth. As in the case of wind-induced acceleration, the ocean pressure gradient force is mostly

645   perpendicular to the iceberg trajectory and therefore does little work on the iceberg.

646   MEDIUM icebergs are released in the same region as THICK ones and over the same simulated historical period. So

647   we expect that the ocean flow has a similarly important geostrophic component. However, in the case of MEDIUM icebergs

648   (see Figure 7), we have a larger superimposed iceberg-to-ocean relative velocity. Therefore, the net direction of iceberg motion

649   force is less clearly orthogonal to the ocean pressure gradient force. The second major difference between MEDIUM and

650   THICK icebergs is that for MEDIUM ones, a larger fraction of their shorter keel is within the Ekman layer, and hence the

651   ocean drag on MEDIUM icebergs is more strongly influenced by the ageostrophic Ekman spiral in the upper ocean. This

652   contributes to further deviations of the iceberg motion away from the direction of the water column's predominantly

653   geostrophic flow, which otherwise would have been purely orthogonal to the iceberg's trajectory. The resulting nonzero

654   projection of the ocean pressure gradient force onto the MEDIUM iceberg trajectories means that this force does work on the

655   icebergs.

656   We furthermore explore the background conditions that give rise to the ocean pressure gradient force. The pre-existing

657   NEMO iceberg module represented the pressure gradients as a function of SSH alone. We analyse our new simulations with

658   the updated algorithms. Our results show that under realistic historical initial and boundary conditions, horizontal density

659   gradients in the ocean exert a noticeable impact on horizontal spatial variability in pressure (Figure 7 and Figure 8) and hence

660   iceberg accelerations in the Amundsen Sea. For MEDIUM ones, horizontal density gradients contribute a smaller component

661   of the full pressure gradient force. This decomposition of pressure, however, is averaged over multiple icebergs and timesteps.

662   The orientation and dominance of the density and SSH gradients varies across timesteps of the simulation and individual

663   icebergs.

664
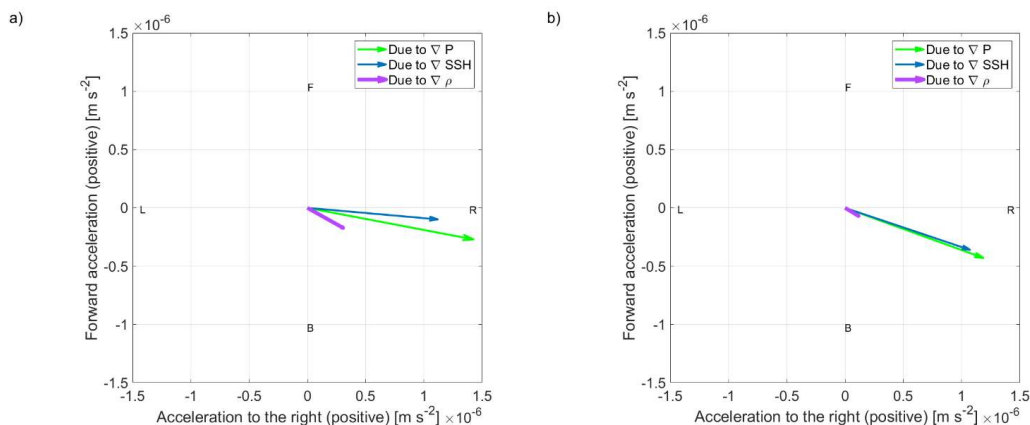
Figure 8: a) same as Figure 6f but for the contributions of SSH and density gradients to the acceleration due to pressure gradients acting on THICK freely floating icebergs in the box where they were launched (Fig. 1), away from shallow topography and ice-shelves and b) as in a but for freely floating MEDIUM icebergs.

4.2 Force balance of grounded icebergs

We now explore the force balance of grounded icebergs. In order to better understand the iceberg-bathymetry interactions, we first run a short NONDISSIPATIVE simulation without sediment resistance or solid-body friction along the bottom. In that case, icebergs whose keels reach the bottom topography are only subject to the force of gravity that pushes them down the slope. If the westward driving accelerations up the eastern flank of Bear Ridge are not large enough to overcome gravity, the icebergs slide eastward down the slope until they resume free flotation. The Coriolis force curves the trajectories of these eastward-moving icebergs northward and then westward, once again pushing them up the slope. This gives rise to a continuous repetitive motion of icebergs up and down the eastern slope of Bear Ridge but also a net northward motion of the bergs parallel to the Ridge (Figure 9). The shape traced out by the iceberg trajectory looks like a stretched-out spiral. Interestingly, such northward displacement of icebergs is indeed observed along Bear Ridge, although not in this unrealistic continuous fashion but instead with intermittent iceberg grounding (see Supplementary Movie).
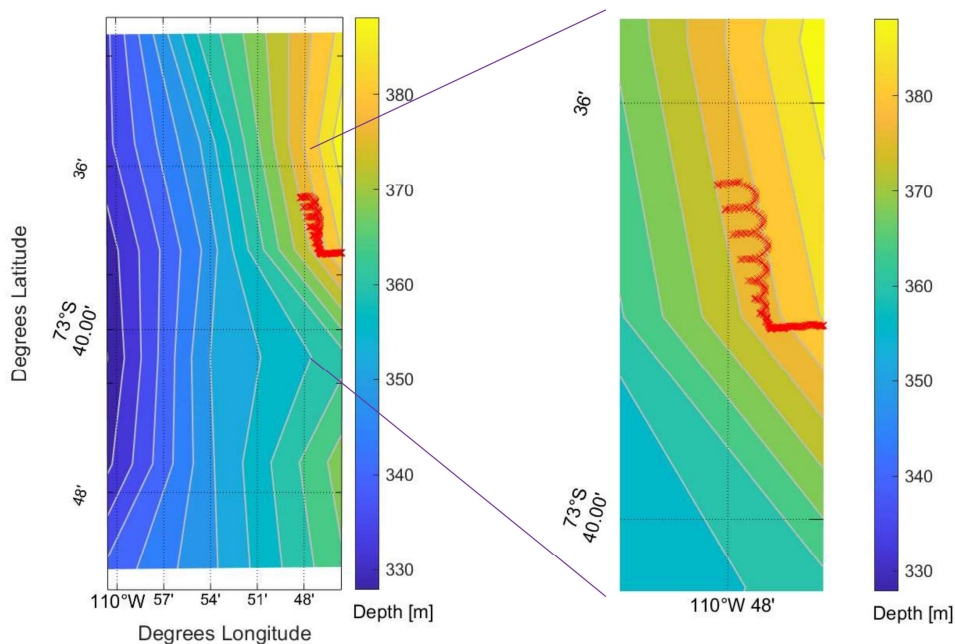
Figure 9: Simulated motion of an iceberg along Bear Ridge in an Amundsen Sea configuration of NEMO without sediment resistance or solid-body friction along the bottom. The topography, with contours 4 m apart in elevation, and the superimposed iceberg trajectory are shown in the Mollweide projection. The right panel shows the enlarged iceberg trajectory. Most of the iceberg trajectory corresponds to a state of free flotation, and the iceberg's vertical displacement along the topographic slope is only on the order of centimeters.
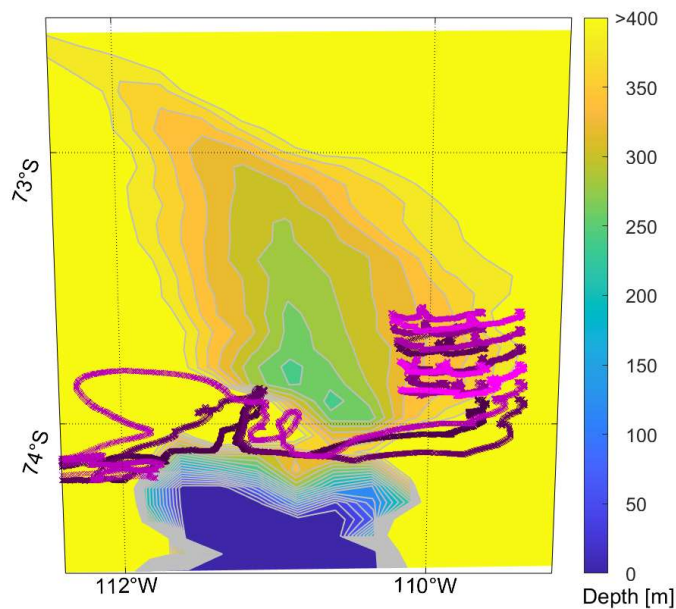
Figure 10: Maps showing 14 iceberg trajectories at 20 minute time-intervals (different shades of purple corresponding to individual icebergs) over the four-year LONG simulation with THICK icebergs, where the colorbar indicates the seafloor depth along Bear Ridge highlighting regions shallower than 400 m. All icebergs in this test are launched east of 109.9° W and north of 74° S.

The second scenario we explore is that along Bear Ridge we impose a uniform 8-m deep layer of sediment with properties observed in the Amundsen Sea, as described in Section 2. We explore this scenario in our Amundsen Sea Simulation

695   LONG. In the LONG simulation with 14 THICK icebergs, three are advected southward and avoid Bear Ridge (Figure 10). A

696   total of 11 icebergs ground on the eastern side of Bear Ridge. In contrast, the keels of MEDIUM icebergs do not extend deep

697   enough to ground along the bottom.

698   In contrast to our NONDISSIPATIVE simulation, in experiment LONG, we have THICK icebergs grounded on Bear

699   Ridge that are subject to sediment resistance. The latter counteracts forces that may otherwise accelerate the icebergs.

700   Occasionally, icebergs also come into contact with the basement and experience Coulomb friction. In this scenario, we do not

701   see a clear northward displacement of the icebergs as they ground and unground. Instead, they come to a stop quite soon after

702   their keels start ploughing scours into the seafloor sediment. The ploughed scours are mostly oriented perpendicular to Bear

703   Ridge and along the zonal direction (Figure 11). The icebergs grounded in the seafloor sediment melt in place, which thins

704   them. In addition, simulated icebergs sporadically receive a strong enough push by the ocean and/or the atmosphere, which

705   allows them to resume their motion briefly and intermittently and to plough scours deeper into the soft sediment (Figure 11b).

706   These ploughing episodes are marked by sporadic short-lived thrusts of acceleration into the sediment (Figure 11) while, most

707   of the time, the icebergs actually remain static when they are embedded in the sediment. This combination of processes creates

708   scours whose depth relative to the surrounding ocean bottom is not uniform or changing monotonically along the scour length

709   but is marked by vertical undulations (Figure 11a), which is reminiscent of the complexity of the observed scours (Figure 2).

710   Note that MEDIUM icebergs have keels that do not reach down to the Bear Ridge topography, and do not scour the bottom;

711   this case was considered solely to examine the force balance of freely floating icebergs.

712

713
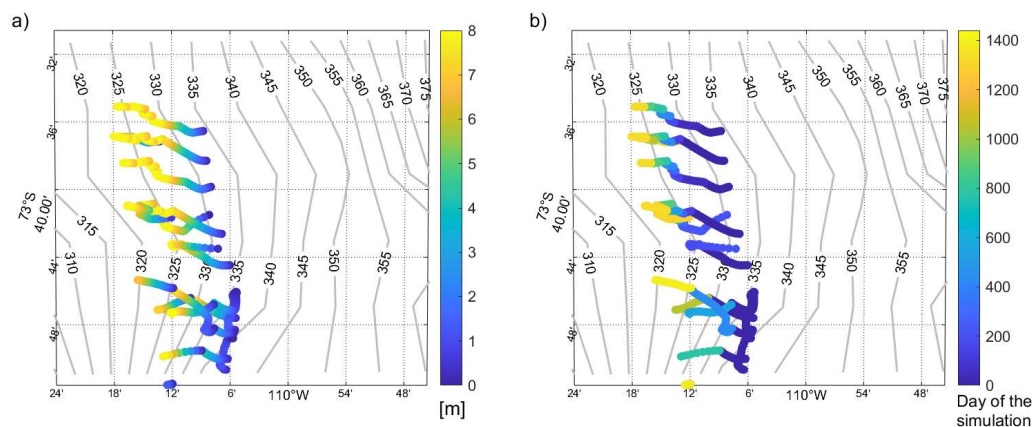
Figure 11: Simulated scours along Bear Ridge from the LONG simulation with THICK icebergs. Panel a shows scour depth [m] and b shows the temporal evolution of the scours [days of the simulation].

716   During the episodes of kinetic grounding, the dominant forces are the sediment resistance, which decelerates the

717   icebergs, and atmospheric drag, which tries to push them forward (Figure 12). The ocean drag also makes a smaller relative

718   contribution towards slowing down kinetically grounded icebergs that plough sediment scours. In the case of kinetic grounding,

719   the force due to ocean drag is much weaker than the pressure gradient force and the Coriolis force. Moreover, the ocean drag

720   does not exhibit a clear prevailing orientation against the direction of motion (Figure 12), and the ocean pressure gradients are

721   not purely orthogonal to the iceberg trajectories. Instead of pointing mostly to the right, as is the case for freely-floating

722   icebergs, the pressure gradient force on kinetically grounded icebergs can point in any of multiple directions. This can be

723   compared with the very clear decelerating effect of ocean drag on freely floating icebergs (Figure 6d). The difference in the

724   relative orientation of the sea-ice drag is noticeable, as well (Figure C1 in Appendix C). When the icebergs are grounded, sea-

725   ice drag acts to push them forward rather than decelerate them or act in a direction orthogonal to their trajectory (Figure C1).

726   Even more importantly, kinetically grounded icebergs experience a large forward push by atmospheric drag. However, the net

727   acceleration, which is also positive, is smaller (Figure 12) due to the large dissipative forces (Figure 13 b,c) where sediment

728   resistance plays a major role (Figure 13). The latter means that while in motion, these kinetically grounded icebergs moving

729   within the sediment and along the bottom topography are rarely in force balance. Note that here we are considering the net

730   acceleration as a weighted average across all four Runge Kutta stages of a given model timestep but before the 'stop' flag

731   described in Section 3.4 is applied. Therefore, the metric in Figure 12e does not include this additional deceleration imposed

732   on icebergs as soon as the condition in equation 21 is fulfilled at any stage of the solver.

733   We furthermore explore the relative contribution of different physical mechanisms to the sediment resistance force

734   and the dominant terms that affect its magnitude (Figure 14). We consider icebergs with an assumed keel width (and hence

735   scour width) W=90m. We see that for scour depths D shallower than 3 m, the shear strength term that is proportional to D

736   dominates over the term due to the weight of the ploughed sediment in accordance with equation 11. In the deeper scours, the

737   density of the ploughed sediment determines to a large extent the total resistance experienced by a grounded iceberg. However,

738   the leading density and shear terms remain comparable for scour depths of 8 m. These results indicate that knowledge of both

739   the sediment density and the shear strength are necessary for an accurate estimate of the sediment resistance experienced by

740   grounding icebergs. On the other hand, the third component of equation (11), which is independent of keel width, remains

741   negligible for all scour depths when the scour width is W=90m. The scour width (which matches the keel width) must be

742   comparable to the scour depth for all three sediment resistance terms to be characterized by the same order of magnitude, and

743   this is not seen in the observations (Figure 2). However, such narrow scours are not resolvable in our observational dataset

744   (Table 1) and could occur in some settings.

745
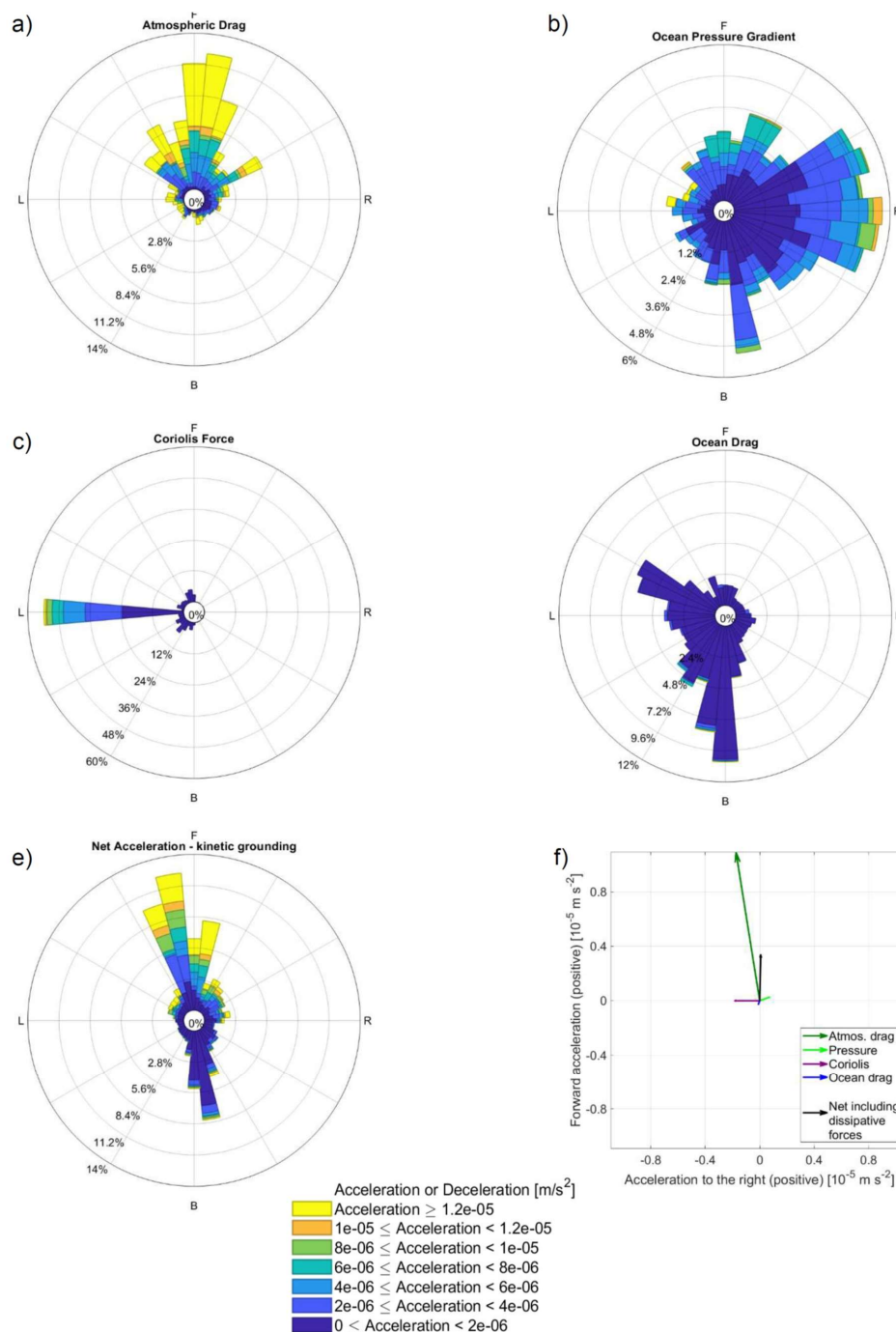
Figure 12: As Figure 6 and 7 and with the same colorscale but for the case of kinetic grounding of THICK icebergs. The net term in (e) is dominated by the dissipative forces shown in Figure 13. Occasionally, the orientation of the Coriolis force is not strictly to the left of the iceberg motion for numerical reasons: the force is calculated using the projected directions of future motion at each Runge-Kutta stage of the iceberg dynamics algorithm.

When icebergs plough all the way to the basement, they experience Coulomb friction and down-slope gravitational acceleration (Figure 13). These additional forces bring icebergs to a halt within one day of contact with the basement, and the icebergs are no longer kinetically grounded.

25

754   We draw a distinction between the term kinetic "grounding" which may still allow for motion along the bottom and

755   a static regime which implies no motion of the grounded iceberg. Icebergs do come to a complete stop even before their keels

756   plough deep enough to reach the solid basement beneath the sediment. In that case, sediment resistance balances the net

757   potential drivers of iceberg motion.

758   When the iceberg keels plough deep into the sediment and eventually reach the basement beneath, they start to feel

759   the effect of Coulomb friction and gravity. Our chosen kinetic Coulomb coefficient value of $\mu = 0.002$ is large enough to

760   bring icebergs rapidly to a halt once they reach the basement along Bear Ridge. In our simulation, we find that when the

761   icebergs reach the basement, they come to a complete stop within the same day and enter a static regime. In this regime, to a

762   first order, static Coulomb friction ($\mu_{stat} = 0.2$) balances the gravitational acceleration that tries to pull the icebergs down the

763   slope (Figures 15 and 16). When the icebergs are statically grounded on the solid basement, Coulomb friction dominates, while

764   sediment resistance and other forces play a less prominent role (compare the orders of magnitude in Figures 13 and 16).

765   During the first year of the LONG simulation with THICK icebergs, the curvature term $\vec{a}_{cuvature}$ in each horizontal

766   direction has a nonnegligible magnitude ($> 1 \times 10^{-6}\ \mathrm{m\ s^{-2}}$) only over the course of less than 23 hours. During the times

767   when the geometric curvature term is greater than $1 \times 10^{-6}\ \mathrm{m\ s^{-2}}$ in magnitude, solid-body friction and gravitational

768   acceleration dominate. We also explore a range of values for the Coulomb coefficient μ, and they also give qualitatively similar

769   results (Appendix B).

770

4.3 Comparison with observations

772 We next consider simulated iceberg residence times along Bear Ridge and qualitatively compare them with observations of

773 the real Amundsen Sea. This allows us to test the fidelity of our new algorithms and the validity of the assumptions we have

774 made regarding sediment and scour properties along Bear Ridge. We furthermore compare our new results with the output of

775 a pre-existing iceberg grounding algorithm in NEMO.
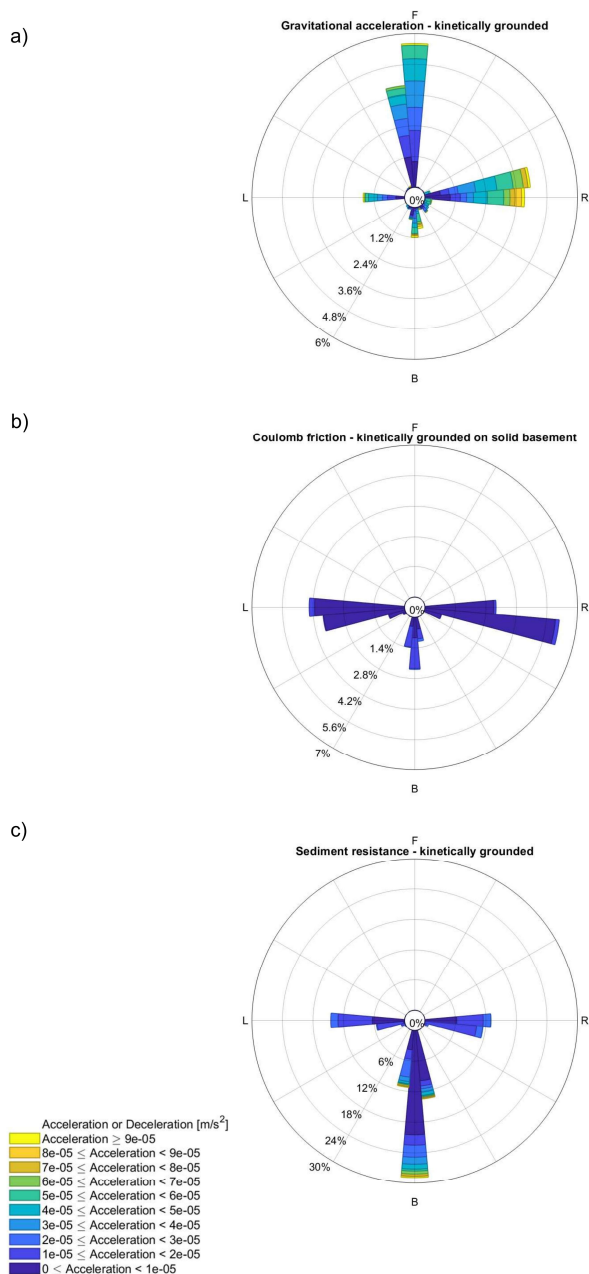
776

777

778

779

780

781

782

783

a)

b)

c)

Figure 13: As Figure 12 and but for the gravitational acceleration and the dissipative forces in the case of kinetic grounding of THICK icebergs: (a) gravitational acceleration present in a small fraction of the iceberg timestep samples (b), the Coulomb solid-body frictional deceleration (c), sediment resistance. Occasionally, the orientation of the sediment resistance force is not strictly against the iceberg motion for numerical reasons: the force is calculated using the projected directions of future motion at each Runge-Kutta stage of the iceberg dynamics algorithm.

790
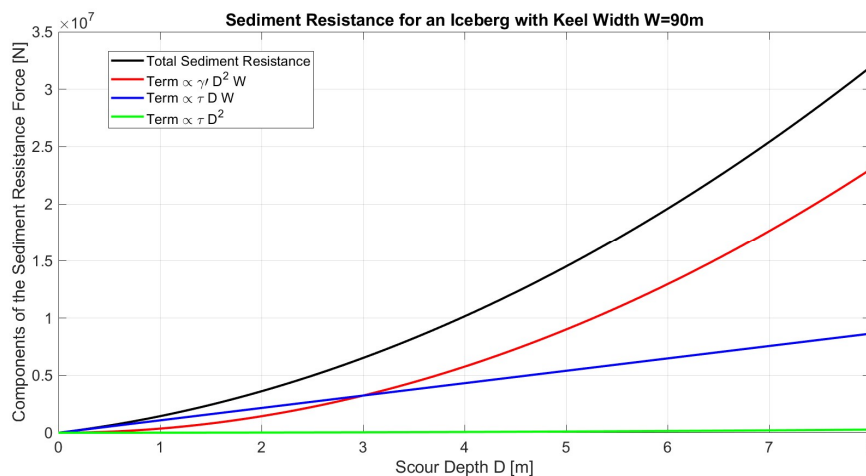
Figure 14: Components of the sediment resistance force [N] as a function of the scour depth D [m] for icebergs with keel width W=90m and sediment properties typical of the Amundsen Sea. The individual terms and their sum   refer   to   equations   6 through 11.

794 In particular, we consider a pre-existing very simple iceberg grounding scheme in which icebergs whose keels reach

795 topography are moved back to their previous floating position and have their horizontal velocity set to zero (Olivé Abelló et

796 al., in prep. and Figure 17a). We apply this algorithm in the SIMPLE GROUNDING simulation with THICK icebergs, and we

797 find that bergs along Bear Ridge quickly leave the region and float away consistent with the simulations of are moved back to

798 their previous floating position and have their horizontal velocity set to zero (Olivé Abelló et al., in prep. If the icebergs do

799 'ground', that grounding is often near the ice shelf fronts. If our pressure gradient algorithm masks the ice shelves, as described

800 in section 3.4, then we see that we avoid trapping as many icebergs near the ice shelf edges (Figure 17b). In that case most

801 icebergs that we launch go around the northern side of the shallow Bear Ridge and quickly end up in the western Amundsen

802 Sea, within a month. Five icebergs circumvent the shallowest part of Bear Ridge by going around its southern end. However,

803 the SIMPLE GROUNDING scheme still remains fundamentally unable to keep the icebergs grounded along Bear Ridge for

804 long enough (Figure 17b).

805 In contrast, with our new updated grounding algorithm, THICK icebergs remain trapped along Bear Ridge for years

806 (Figure 17c). Crucially, assuming a deformable sediment layer above the basement is what allows the icebergs to remain

807 grounded along Bear Ridge (Figure 17 and Appendix B). This stands in contrast to the rapid northward export of icebergs in

808 the scenario without seafloor sediments or solid-body friction (compare Figures 9 against 10, 11 and 17). While icebergs in

809 the real Amundsen Sea do propagate northward, they also remain grounded for long periods of time suggesting that frictional

810 forces are an important consideration and should be retained in the model. Our results are in qualitative agreement with the

811 observations suggesting that thick icebergs may be trapped on Bear Ridge for months or years.

812 Our results are also robust with respect to the choice of value for the Coulomb coefficients μ and μ_{stat} (Appendix

813 B). We find that varying the magnitude of μ does not affect the episodes of motionless grounding (Figure B1 in Appendix B).

814 In contrast, the static episodes marked appear to be more influenced by the sediment resistance and the processes that thin the
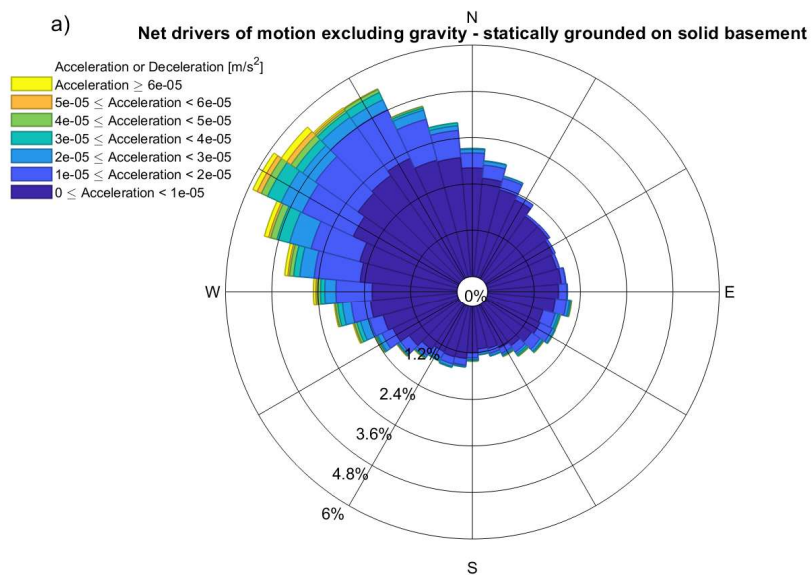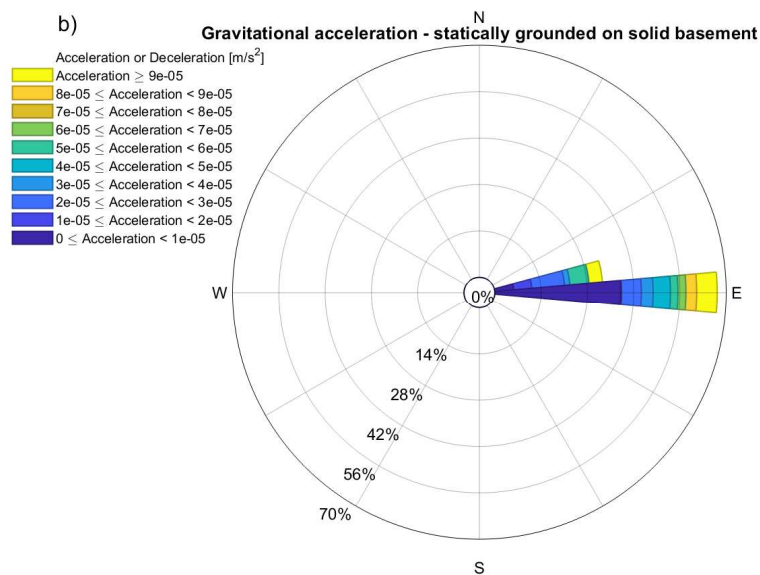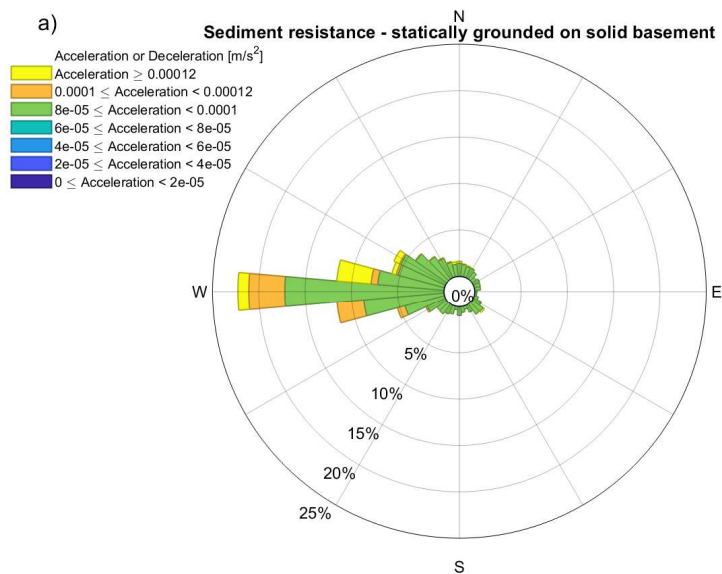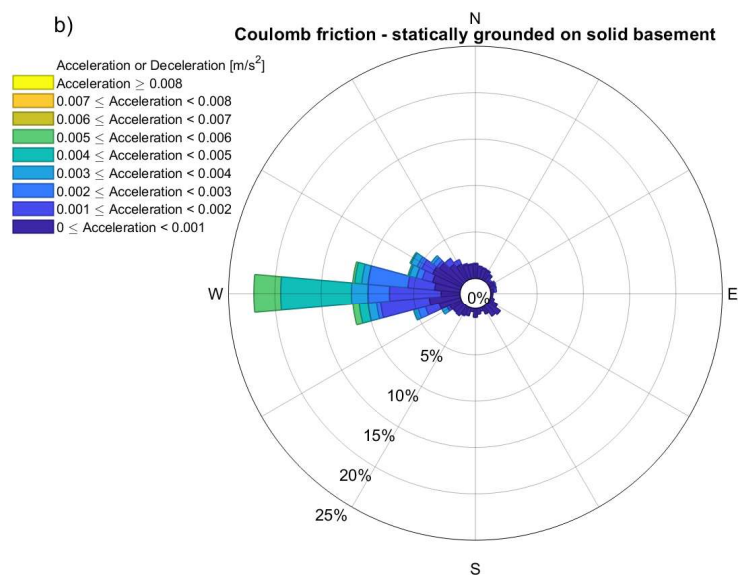
815 icebergs.

816

817

818

819

820

821

822

823

824

Figure 15: As Figure 12 and 13 but for the net acceleration excluding gravity (a) and the gravitational acceleration (b) in the case of static grounding of THICK icebergs on solid basement. Note that unlike Figures 12-13, the directions are here the cardinal points as the icebergs do not move.

825
826
827

a)

Sediment resistance - statically grounded on solid basement

b)

Coulomb friction - statically grounded on solid basement

Figure 16: As Figure 15 but for the dissipative forces due to sediment resistance (a) and static Coulomb friction (b) in the case of static grounding of THICK icebergs in the case of grounding along the basement, the icebergs in the simulation always come to rest and enter a static regime. The static Coulomb frictional deceleration shown here is the maximum achievable magnitude, but the effective friction does not exceed the sum of the other sources of acceleration, which are dominated by gravity.

30

834

835
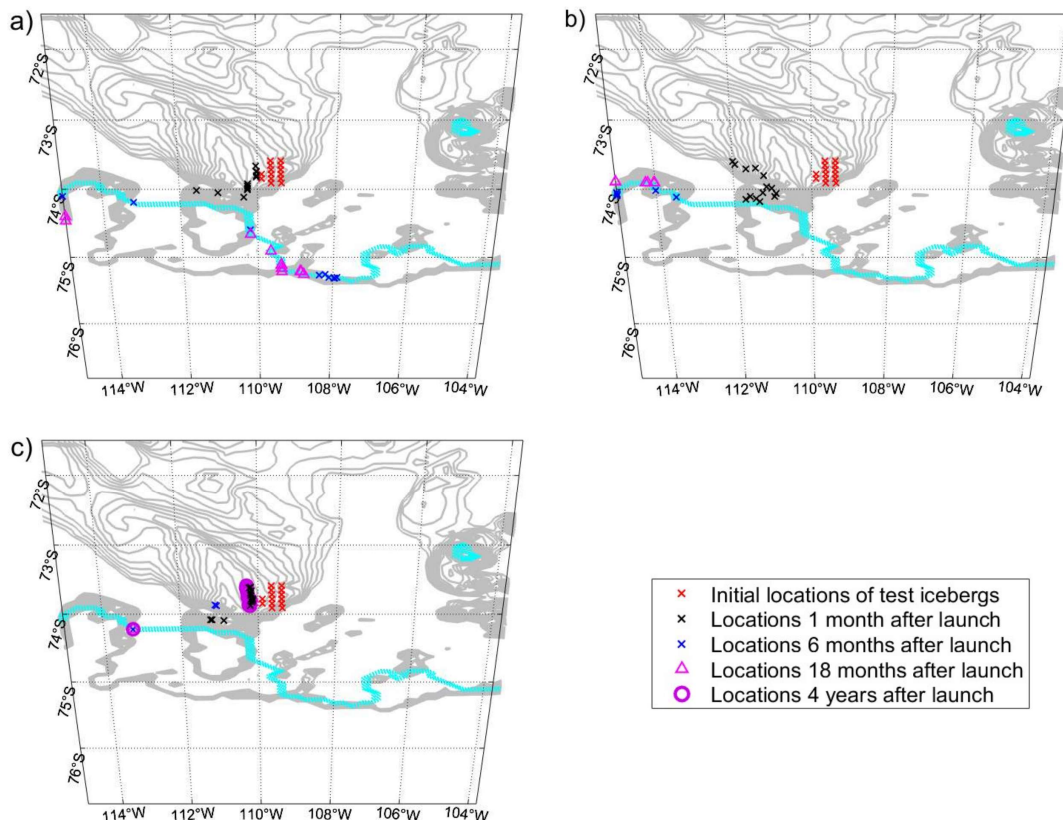
Figure 17: Locations of THICK icebergs during the course of the (a) pre-existing SIMPLE GROUNDING; (b) the pre-existing SIMPLE GROUNDING scheme and with masked pressure gradient forces along the iceshelf edge; and (c) LONG dissipative simulation with the new grounding scheme. The topography shallower than 560 m is superimposed with gray contours, 20 m apart. The blue line denotes the ice shelf fronts, where many icebergs come to a stop under the pre-existing SIMPLE GROUNDING scheme. Iceberg locations 4 years after launch are shown for the simulation with new grounding scheme only.

5 Summary and conclusions

We have introduced a new and improved representation of iceberg dynamics and iceberg grounding capability in NEMO. These updates to the model are verified using idealized test configurations before being applied to an eddy-permitting regional simulation of the Amundsen Sea forced with historical boundary conditions. We note that in this initial study our specific intention is to develop the new model physics, and so we delay a full multi-year realistic simulation of iceberg calving and grounding to a subsequent study. A companion paper presents an improved iceberg thickness distribution in NEMO based on the thickness of the Antarctic ice-shelves from which icebergs calve (Olivé Abelló et al., in prep.). The companion paper also introduces an objective definition of iceberg size classes implemented in NEMO (Olivé Abelló et al., in prep.). Future work will combine these two approaches. Once we are in possession of a full realistic simulation, a much fuller comparison to observed iceberg grounding can take place, with additional tuning of the iceberg grounding parameters. This would also require the application of advanced techniques for tracking iceberg grounding episodes from satellite imagery, perhaps involving artificial intelligence (AI) techniques. A full comparison of simulated and observed iceberg scours would also be extremely powerful in constraining the model.

854   The Amundsen Sea experiments suggest that in this region the ocean pressure gradients acting on icebergs are not

855   always determined solely by spatial variability in SSH. Instead, our results highlight the important direct contribution of

856   horizontal gradients in the ocean density, which separate from the contribution of density through steric SSH variability. In

857   addition, we show that large freely drifting tabular icebergs in the Amundsen Sea often enter a dynamical regime characterized

858   as a force balance between surface winds and the Coriolis force. During episodes of intense winds, ocean drag counteracts the

859   stress exerted by the atmosphere on icebergs. In contrast, smaller icebergs experience stronger turbulent ocean drag. Overall,

860   large freely floating tabular icebergs in the Amundsen Sea are not subject to strong net acceleration along or against their

861   direction of motion, but tend to get deflected to the left by Coriolis force. This is consistent with the theoretical arguments

862   presented by Wagner et al. (2017) who suggest a similar balanced regime for large tabular icebergs when the ocean is in a

863   purely geostrophic regime. In our new theoretical analysis, we have also been able to derive more general scaling arguments

864   that describe the momentum budget of large and medium icebergs even in the presence of significant and realistic ageostrophic

865   Ekman flow.

866   Our results for the force balance of freely floating icebergs also highlight the potential dynamical importance of

867   iceberg fragmentation. If large and thick tabular icebergs get fragmented, the smaller fragments will get advected in a different

868   direction compared to a parent iceberg that remains intact. Under identical oceanic and atmospheric conditions, large and small

869   icebergs originating from the same place ultimately drift towards and melt in different geographical locations. Furthermore,

870   our results for the dependence of the turbulent iceberg-ocean drag on iceberg size have implications for the rate of iceberg

871   subsurface melting. Jenkins et al. (2010) and Davis et al. (2023) point out that the rate of ice shelf basal melting depends on

872   the velocity beneath the shelf. By analogy, the rate of iceberg subsurface melting, especially for large tabular icebergs, should

873   exhibit a similar dependence on the relative iceberg-ocean velocity and turbulent drag. We have shown that the latter vary

874   strongly with the iceberg size. This once again points to the potential importance of the fragmentation of large icebergs into

875   smaller ones, which is not presently represented in NEMO or in our updated algorithms.

876   Our new algorithms show how the force balance is altered when icebergs interact with the ocean bottom. The new

877   grounding representation in NEMO allows us to reproduce realistic bottom scours and grounding along Bear Ridge in the

878   Amundsen Sea. We compare our simulations against observations in the region. If the seafloor is characterised by deformable

879   sediments, then the grounding process is marked by alternating periods of slowdown and arrest followed by episodic

880   acceleration that thrusts the icebergs deeper into the sediment (Figure 11). The sediment resistance force is characterized by

881   comparable contributions due to the density and the shear strength of the deformable layer. Consistent with observations, the

882   presence of a sediment layer in our simulations allows thick icebergs to remain trapped along Bear Ridge on a timescale of

883   years (Figure 17c) despite their susceptibility to basal and lateral melting. The long residence time of icebergs along the Ridge

884   and their eventual northward motion affect the distribution of iceberg meltwater (Bett et al., 2020) but also, more importantly,

885   create the Amundsen Sea Polynya and the dipole in the distribution of sea ice growth on either side of Bear Ridge. In contrast,

886   the absence of sediment resistance and solid-body friction with the basement would give rise to conditions that continuously

887   drive icebergs northward along the eastern slope of Bear Ridge.

888   The new model algorithms implemented in this study will allow us to explore the existence of possible feedback

889   mechanisms between iceberg grounding along Bear Ridge in the Amundsen Sea and the calving of new icebergs from the shelf

890   under changing climate conditions, as suggested by Bett et al. (2020). Ultimately, it will allow these processes to be more

891   accurately represented circumpolarly, with consequent improvements in regional ocean representation, particularly over the

892   continental shelves. Presently, this is a region that models struggle to accurately recreate, notably the interactions between

893   melt and sea ice distribution, polynyas, dense shelf water formation and wider ocean vertical circulation (e.g. Aguiar et al.,

894   2024). The strength of this mechanism and its future response to projected climate change have important implications for the

895   freshwater budget of the Amundsen Sea, for the stability of ice shelves, and ultimately, for global sea level rise.

896

897 **References**

898 Aguiar, W., Lee, S.-K., Lopez, H., Dong, S., Seroussi, H., Jones, D. C., & Morrison, A. K. (2023). Antarctic Bottom Water
899 sensitivity to spatio-temporal variations in Antarctic meltwater fluxes. Geophysical Research Letters, 50, e2022GL101595.
900 https://doi.org/10.1029/2022GL101595

901

902 Arrigo, K.R., Lowry, K.E., and van Dijken, G.L. (2012) Annual changes in sea ice and phytoplankton in polynyas of the
903 Amundsen Sea, Antarctica, Deep Sea Res. Part II: Topical Studies in Oceanography, Vol. 71–76, 5-15,
904 https://doi.org/10.1016/j.dsr2.2012.03.006.

905

906 Asay-Davis, X. S., Cornford, S. L., Durand, G., Galton-Fenzi, B. K., Gladstone, R. M., Gudmundsson, G. H., Hattermann, T.,
907 Holland, D. M., Holland, D., Holland, P. R., Martin, D. F., Mathiot, P., Pattyn, F., and Seroussi, H.: Experimental design for
908 three interrelated marine ice sheet and ocean model intercomparison projects: MISMIP v. 3 (MISMIP +), ISOMIP v. 2
909 (ISOMIP +) and MISOMIP v. 1 (MISOMIP1), Geosci. Model Dev., 9, 2471–2497, https://doi.org/10.5194/gmd-9-2471-2016,
910 2016.

911

912 Barnes, P. W., and R. Lien (1988), Icebergs rework shelf sediments to 500-m off Antarctica, Geology, 16(12), 1130–1133.

913

914 Bass DW. Stability of Icebergs. Annals of Glaciology. 1980; 1:43-47. doi:10.3189/S0260305500016943

915

916 Bett, D. T., et al. (2020) The impact of the Amundsen Sea freshwater balance on ocean melting of the West Antarctic Ice
917 Sheet. *JGR: Oceans*, https://doi.org/10.1029/2020JC016305

918

919 Bigg GR, et al. 1996. Prediction of iceberg trajectories for the North Atlantic and Arctic oceans. Geophys. Res. Lett.
920 23:243587–90

921

922 Bigg, G.R., et al. (1997) Modelling the dynamics and thermodynamics of icebergs, Cold Regions Science and Technology,
923 Vol. **26**, 2, 113-135, https://doi.org/10.1016/S0165-232X(97)00012-8

924 Bigg, G.R., Cropper, T.E., O'Neill, C.K. *et al.* A model for assessing iceberg hazard. *Nat Hazards* **92**, 1113–1136 (2018).
925 https://doi.org/10.1007/s11069-018-3243-x

926 Christopher S. Brown, Andrew M.W. Newton, Mads Huuse, Francis Buckley, Iceberg scours, pits, and pockmarks in the North
927 Falkland Basin, Marine Geology, Volume 386, 2017, Pages 140-152, https://doi.org/10.1016/j.margeo.2017.03.001.

928

929 Caillet, Justine & Jourdain, Nicolas & Mathiot, Pierre & Hellmer, Hartmut & Mouginot, Jérémie. (2022). Drivers and
930 Reversibility of Abrupt Ocean State Transitions in the Amundsen Sea, Antarctica. Journal of Geophysical Research: Oceans.
931 128. 10.1029/2022JC018929.

932

933 Cefarelli, Adrián & Ferrario, Martha & Vernet, Maria. (2016). Diatoms (Bacillariophyceae) associated with free-drifting
934 Antarctic icebergs: taxonomy and distribution. Polar Biology. 39. 10.1007/s00300-015-1791-z.

935

936 Cenedese, C. and Straneo, F. Icebergs Melting. *Annu. Rev. Fluid Mech.* 2023. 55:377–402

937

938 Chari, T. R. (1975) Some geotechnical aspects of iceberg grounding. Doctoral (PhD) thesis, Memorial University of
939 Newfoundland

940

941 Chari, T.R. et al. (1980) Environmental factors affecting iceberg scour estimates, Cold Regions Sci. and Tech.,DOI:
942 https://doi.org/10.1016/0165-232X(80)90050-6.

943

944 R.W. Clark, J.S. Wellner, C. Hillenbrand, R.L. Totten, J.A. Smith, L.E. Miller, R.D. Larter, K.A. Hogan, A.G.C. Graham,
945 F.O. Nitsche, A.A. Lehrmann, A.P. Lepp, J.D. Kirkham, V.T. Fitzgerald, G. Garcia-Barrera, W. Ehrmann, and L. Wacker,
946 (2024) Synchronous retreat of Thwaites and Pine Island glaciers in response to external forcings in the presatellite era, *Proc.*
947 *Natl. Acad. Sci. U.S.A.* 121 (11) e2211711120, https://doi.org/10.1073/pnas.2211711120.

948 Condron, A., Hill, J.C. Timing of iceberg scours and massive ice-rafting events in the subtropical North Atlantic. Nat
949 Commun 12, 3668 (2021). https://doi.org/10.1038/s41467-021-23924-0

950

951 Davis, P.E.D., Nicholls, K.W., Holland, D.M. *et al.* Suppressed basal melting in the eastern Thwaites Glacier grounding
952 zone. *Nature* **614**, 479–485 (2023). https://doi.org/10.1038/s41586-022-05586-0

953

954 Davison BJ, Hogg AE, Gourmelen N, Jakob L, Wuite J, Nagler T, Greene CA, Andreasen J, Engdahl ME. (2023) Annual mass
955 budget of Antarctic ice shelves from 1997 to 2021. *Sci Adv.* Oct 13; 9(41):eadi0186. doi: 10.1126/sciadv.adi0186

956

957 Darwin, C. R. 1855. On the power of icebergs to make rectilinear uniformly-directed grooves across a submarine undulatory
958 surface. *The London, Edinburgh and Dublin Philosophical Magazine* *10*(64), 96–98.
959 https://doi.org/10.1080/14786445508641938

960

961 Dowdeswell, J. A., and Bamber J. L. (2007), Keel depths of modern Antarctic icebergs and implications for sea-floor scouring
962 in the geological record, Marine Geology, 243**,** 120-131.

963 Pierre Dutrieux *et al.*, Strong Sensitivity of Pine Island Ice-Shelf Melting to Climatic Variability. *Science* **343**,174-178 (2014).
964 DOI:10.1126/science.1244341

965 Smith, J.A., Claus-Dieter Hillenbrand, Gerhard Kuhn, Robert D. Larter, Alastair G.C. Graham, Werner Ehrmann, Steven G.
966 Moreton, Matthias Forwick, Deglacial history of the West Antarctic Ice Sheet in the western Amundsen Sea Embayment,
967 *Quaternary Science Reviews*, Volume 30, Issues 5-6,2011, Pages 488-505, https://doi.org/10.1016/j.quascirev.2010.11.020

968

969 FitzMaurice, A., F. Straneo, C. Cenedese, and M. Andres (2016), Effect of a sheared flow on iceberg motion and
970 melting*, Geophys. Res. Lett.*, **43**, 12,520–12,527, doi:10.1002/2016GL071602.

971 Fowler AC. Weertman, Lliboutry and the development of sliding theory. *Journal of Glaciology*. 2010;56(200):965-972.
972 doi:10.3189/002214311796406112

973

974 Fox-Kemper B, Adcroft A, Böning CW, Chassignet EP, Curchitser E, Danabasoglu G, Eden C, England MH, Gerdes R,
975 Greatbatch RJ, Griffies SM, Hallberg RW, Hanert E, Heimbach P, Hewitt HT, Hill CN, Komuro Y, Legg S, Le Sommer J,

976   Masina S, Marsland SJ, Penny SG, Qiao F, Ringler TD, Treguier AM, Tsujino H, Uotila P and Yeager SG (2019) Challenges
977   and Prospects in Ocean Circulation Models. *Front. Mar. Sci.* 6:65. doi: 10.3389/fmars.2019.0006
978
979   Gladstone, Rupert M.; Bigg, Grant R.; Nicholls, Keith W. 2001 Iceberg trajectory modeling and meltwater injection in the
980   Southern Ocean. *Journal of Geophysical Research*, 106 (C9). 19,903-19,915. https://doi.org/10.1029/2000JC000347
981
982   Graham, A.G.C., Larter, R.D., Gohl, K., Hillenbrand, C.-D., Smith, J.A., and Kuhn, G. (2009), Bedform signature of a West
983   Antarctic palaeo-ice stream reveals a multi-temporal record of flow and substrate control, Quaternary Science Reviews, 28,
984   2774-2793.
985
986   Hawkings, J. R., Wadham, J. L., Benning, L. G., Hendry, K. R., Tranter, M., Tedstone, A., Nienow, P., & Raiswell, R. (2017).
987   Ice sheets as a missing source of silica to the polar oceans. *Nature Communications*, 8, Article 14198.
988   https://doi.org/10.1038/ncomms14198
989
990   Hopwood MJ, Carroll D, Höfer J, Achterberg EP, Meire L, Le Moigne FAC, Bach LT, Eich C, Sutherland DA, González HE.
991   Highly variable iron content modulates iceberg-ocean fertilisation and potential carbon export. *Nat Commun.* 2019 Nov
992   20;10(1):5261. doi: 10.1038/s41467-019-13231-0.
993   Lopez, R. et al., Hydrodynamic Effects On Iceberg Gouging. *Cold Regions Science and Technology*, 4 (1981) 55-61 55
994
995   Jacobs, S., A. Jenkins, H. Hellmer, C. Giulivi, F. Nitsche, B. Huber, and R. Guerrero. 2012. The Amundsen Sea and the
996   Antarctic Ice Sheet. *Oceanography* 25(3):154–163, https://doi.org/10.5670/oceanog.2012.90.
997
998   Jakobsson, M., et al. (2011), Geological record of ice shelf break-up and grounding line retreat, Pine Island Bay, West
999   Antarctica, Geology, 39(7), 691–694.
1000
1001   Jenkins, A., K. W. Nicholls, and H. F. J. Corr, 2010: Observation and Parameterization of Ablation at the Base of Ronne Ice
1002   Shelf, Antarctica. *J. Phys. Oceanogr.*, **40**, 2298–2312, https://doi.org/10.1175/2010JPO4317.1.
1003
1004   Jourdain, N. C., et al. 2019. Simulating or prescribing the influence of tides on the Amundsen Sea ice shelves, *Ocean
1005   Modelling*, Vol. 133, 44-55, https://doi.org/10.1016/j.ocemod.2018.11.001.
1006
1007   Kostov, Yavor; Holland, Paul R.; Hogan, Kelly A.; Smith, James A.; Jourdain, Nicolas C; Mathiot, Pierre; Olivé Abelló, Anna;
1008   Fleming, Andrew H.; Meijers, Andrew J. S.: Modelled dynamics of floating and grounded icebergs, with application to the
1009   Amundsen Sea. Supplementary Movie. Copernicus Publications, 2025a. https://doi.org/10.5446/70447
1010   Kostov et al. 2025b. Updates to the NEMO iceberg dynamics and grounding (Version 2). Zenodo.
1011   https://doi.org/10.5281/zenodo.15484879
1012   Ian Joughin *et al.*, Ice-shelf retreat drives recent Pine Island Glacier speedup. *Sci. Adv.***7**, eabg3080 (2021).
1013   DOI:10.1126/sciadv.abg3080
1014   Lemieux, J.-F., F. Dupont, P. Blain, F. Roy, G. C. Smith, and G. M. Flato (2016), Improving the simulation of landfast ice by
1015   combining tensile strength and a parameterization for grounded ridges, J. Geophys. Res. Oceans, 121, 7354–7368,
1016   doi:10.1002/2016JC012006.

1017   Lien, R., A. Solheim, A. Elverhoi, and K. Rokoengen (1989), Iceberg scouring and sea bed morphology on the eastern Weddell

1018   Sea shelf, Antarctica, Polar Research, 7(1), 43–57.

1019

1020   Lucas, N., Brearley, J., Katherine Hendry et al. Giant icebergs increase mixing and stratification in upper-ocean layers, 10

1021   June 2024, PREPRINT (Version 1) available at Research Square [https://doi.org/10.21203/rs.3.rs-4425629/v1]

1022

1023   Madec, G., & NEMO-Team. (2016). Note du Pôle de modélisation de l'Institut Pierre-Simon Laplace No 27. In *NEMO ocean*

1024   *engine, version 3.6 stable (Technical Report)*. France: IPSL.

1025

1026   Madec, G., & NEMO System Team. (2022). NEMO ocean engine. *Zenodo*. **https://doi.org/10.5281/zenodo.6334656**

1027

1028   Marsh, R.; Ivchenko, V.O.; Skliris, N.; Alderson, S.; Bigg, G.R.; Madec, G.; Blaker, A.T. ; Aksenov, Y. ; Sinha, B.; Coward,

1029   A.C. ; Le Sommer, J.; Merino, N.; Zalesny, V.B.. 2015 NEMO–ICB (v1.0): interactive icebergs in the NEMO ocean model

1030   globally   configured   at   eddy-permitting   resolution. *Geoscientific   Model   Development*,   8   (5).   1547-1562.

1031   https://doi.org/10.5194/gmd-8-1547-2015

1032

1033   Marsh, R., Bigg, G., Zhao, Y. et al. Prospects for seasonal forecasting of iceberg distributions in the North Atlantic. Nat

1034   Hazards 91, 447–471 (2018). https://doi.org/10.1007/s11069-017-3136-4

1035

1036   Marson, J. M., Myers, P. G., Garbo, A., Copland, L., & Mueller, D. (2024). Sea ice-driven iceberg drift in Baffin Bay.
1037   *Journal of Geophysical Research: Oceans*, 129, e2023JC020697. https://doi.org/10.1029/2023JC020697
1038

1039   Martin, T. and Adcroft, A. (2010) Parameterizing the fresh-water flux from land ice to ocean with interactive icebergs in a

1040   coupled climate model, Ocean Modelling, Vol. 34, Issues 3–4, 111-124, https://doi.org/10.1016/j.ocemod.2010.05.001

1041

1042   Mazur, A. K., Wahlin, A. K., & Kalén, O. (2019). The life cycle of small-to medium-sized icebergs in the Amundsen Sea

1043   Embayment. *Polar Research*, *38*.

1044

1045   Merino, N., Julien Le Sommer, Gael Durand, Nicolas C. Jourdain, Gurvan Madec, Pierre Mathiot, Jean Tournadre, Antarctic

1046   icebergs melt over the Southern Ocean: Climatology and impact on sea ice, *Ocean Modelling*, Volume 104,2016,Pages 99-

1047   110, https://doi.org/10.1016/j.ocemod.2016.05.001.

1048

1049   Miles BWJ, Stokes CR, Jenkins A, Jordan JR, Jamieson SSR, Gudmundsson GH. Intermittent structural weakening and

1050   acceleration of the Thwaites Glacier Tongue between 2000 and 2018. *Journal of Glaciology*. 2020;66(257):485-495.

1051   doi:10.1017/jog.2020.20

1052

1053   Morlighem,   M.,   Rignot,   E.,   Binder,   T.,   Blankenship,   D.,   Drews,   R.,   Eagles,   G.,   et al.   (2020). Deep   glacial   troughs   and

1054   stabilizing   ridges   unveiled   beneath   the   margins   of   the   Antarctic   ice   sheet. Nature   Geoscience, 13(2), 132–

1055   137. https://doi.org/10.1038/s41561-019-0510-8

1056

1057   Mouginot, J., E. Rignot, and B. Scheuchl (2014), Sustained increase in ice discharge from the Amundsen Sea Embayment,

1058   West Antarctica, from 1973 to 2013, *Geophys. Res. Lett.*, 41, 1576–1584, doi:10.1002/2013GL059069.

1059

1060 Naughten, K. A., Holland, P. R., Dutrieux, P., Kimura, S., Bett, D. T., & Jenkins, A. (2022). Simulated twentieth-century
1061 ocean warming in the Amundsen Sea, West Antarctica. *Geophysical Research Letters*, 49,
1062 e2021GL094566. https://doi.org/10.1029/2021GL094566

1064 Nakayama, Y. , Timmermann, R. , Schröder, M. and Hellmer, H. (2014): On the difficulty of modeling Circumpolar Deep
1065 Water intrusions onto the Amundsen Sea continental shelf , *Ocean Modelling*, 84 , pp. 26-34 . doi:
1066 10.1016/j.ocemod.2014.09.007

1068 Olivé Abelló, A., Mathiot, P. Jourdain, N.C., Kostov, Y., Holland, P. R. Gascoin S., and Rousset C. (2025) Iceberg grounding
1069 enhances the release of freshwater on the Antarctic continental shelf. Submitted to JGR-Oceans

1071 Ruffman, A. (2005) The First Known Attempts Off Eastern Canada 'to Tow, or Cant' Icebergs: a seed to the understanding of
1072 iceberg scour processes at the seafloor. CMOS Bulletin SCMO. Vol. 33, 99-123http://cmosarchives.ca/Bulletin/b3304.pdf

1073 Shepherd, A., Gilbert, L., Muir, A. S., Konrad, H., McMillan, M., Slater, T., et al. (2019). Trends in Antarctic Ice Sheet
1074 elevation and mass. *Geophysical Research Letters*, 46, 8174–8183. https://doi.org/10.1029/2019GL082182

1075 Stern, A. A., A. Adcroft, and O. Sergienko (2016), The effects of Antarctic iceberg calving-size distribution in a global climate
1076 model, *J. Geophys. Res. Oceans*, 121, 5773– 5788, doi:10.1002/2016JC011835.

1077 St-Laurent, P., J. M. Klinck, and M. S. Dinniman (2015), Impact of local winter cooling on the melt of Pine Island Glacier,
1078 Antarctica, *J. Geophys. Res. Oceans*, 120, 6718–6732, doi:10.1002/2015JC010709

1080 St-Laurent, P., Stammerjohn, S. E., & Maksym, T. (2024). Response of onshore oceanic heat supply to yearly changes in the
1081 Amundsen Sea icescape (Antarctica). *Journal of Geophysical Research: Oceans*, 129,
1082 e2023JC020467. https://doi.org/10.1029/2023JC020467

1084 Tarling, Geraint A. ; Thorpe, Sally E. ; Henley, Sian F.; Burson, Amanda ; Liszka, Cecilia M. ; Manno, Clara ; Lucas, Natasha
1085 S. ; Ward, Freyja; Hendry, Katharine R. ; Woodward, E. Malcolm S.; Wootton, Marianne; Abrahamsen, E. Povl. 2024 Collapse
1086 of a giant iceberg in a dynamic Southern Ocean marine ecosystem: in situ observations of A-68A at South Georgia. *Progress*
1087 *in Oceanography*, 226, 103297. 17, pp. https://doi.org/10.1016/j.pocean.2024.103297

1089 Tsujino, H., et al. (2018) JRA-55 based surface dataset for driving ocean–sea-ice models (JRA55-do), Ocean Modelling, Vol.
1090 130, 79-139, https://doi.org/10.1016/j.ocemod.2018.07.002.

1092 Veldhuijsen, S. B. M., van de Berg, W. J., Brils, M., Kuipers Munneke, P., and van den Broeke, M. R.: Characteristics of the
1093 1979–2020 Antarctic firn layer simulated with IMAU-FDM v1.2A, The Cryosphere, 17, 1675–1696,
1094 https://doi.org/10.5194/tc-17-1675-2023, 2023.

1096 Wagner, T. J. W., R. W. Dell, and I. Eisenman, 2017: An Analytical Model of Iceberg Drift. *J. Phys. Oceanogr*., 47, 1605–
1097 1616, https://doi.org/10.1175/JPO-D-16-0262.1.

1099 Wise, M.G., Dowdeswell, J.A., Jakobsson, M.J., and Larter, R.D. (2017), Evidence of marine ice-cliff instability in Pine Island
1100 Bay from iceberg-keel plough marks, Nature, 550(7677), 506-510.

Code availability

1102 The updated code for the NEMO iceberg module is publicly available at the following repository
1103 https://doi.org/10.5281/zenodo.15484879
1104

1115

Appendix A. Supplementary Movie

1117 We enclose a hyperlink (https://doi.org/10.5446/70447) to a supplementary movie composed of Copernicus Sentinel-1 SAR
1118 (synthetic aperture radar) images taken over the time period 2017-2024, an extension of the movie provided in Bett et al.
1119 (2020). The movie highlights the locations of grounded icebergs of various sizes along the shallow Bear Ridge. Many of the
1120 still images in the movie also show the dipole in sea-ice concentration with larger values to the east of the Bear Ridge.
1121
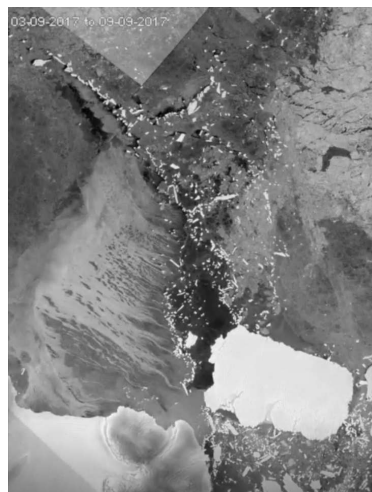
Supplementary Movie A. Available at the TIB AV Portal (Kostov et al., 2025a) : https://doi.org/10.5446/70447

1127

**Appendix B. Effects of topographic curvature, substepping parameters, and the Coulomb coefficient of solid-body friction**

We explore the parameter space of possible values for the unconstrained Coulomb coefficient of solid-body friction μ across different shorter repetitions of the Amundsen Sea Simulation B that extend for more than 350 days. In each case, we vary the coefficient of kinetic friction, while the coefficient of static friction is always set to be 100 times larger than the kinetic one.

We find that varying the value of the kinetic μ and static coefficient μ_{stat} by different orders of magnitude does not affects the statistics for episodes of motionless grounding (Figure B1). We infer two conclusions from this result. First, our results are robust with respect to the unconstrained value of the Coulomb coefficient for solid body friction. Second, the duration of episodes of grounding along the bottom seem to be governed by sediment resistance and melting processes that thin the icebergs.

We also show that in the presence of a sediment layer above the crystalline basement, the detailed parameterization of the interaction with the shape of the topography becomes less important. For example, we see that the effect of topographic curvature does not contribute to qualitative differences in the shape and evolution of iceberg scours (Figure B1). Similarly, using or not using temporal sub-stepping does not play a first order role when icebergs ground in the sediment above the crystalline base (Figure B1).

We do find that having no Coulomb friction (Figure B1) or having neither friction, nor sediment resistance (Figure 9 in the main text) are extreme cases where the absence of processes makes a noticeable difference. If there is no solid-body friction but there is sediment resistance, icebergs plough swirls and half-loops or exhibit a repetitive back and forth motion along the slope (Figure B1). If no dissipative force acts on a grounded iceberg, then its trajectory can trace out a spiral motion (Figure 9 in the main text). Interestingly, iceberg scours in the shape of swirls and spirals are indeed observed along the ocean bottom in the real world, but they are traditionally attributed to the effect of tides (See Figure 2 and Section 2). In our model configurations, we do not represent tidal effects, yet we observe such features and point out the important role of the Coriolis force for driving oscillatory iceberg motion.
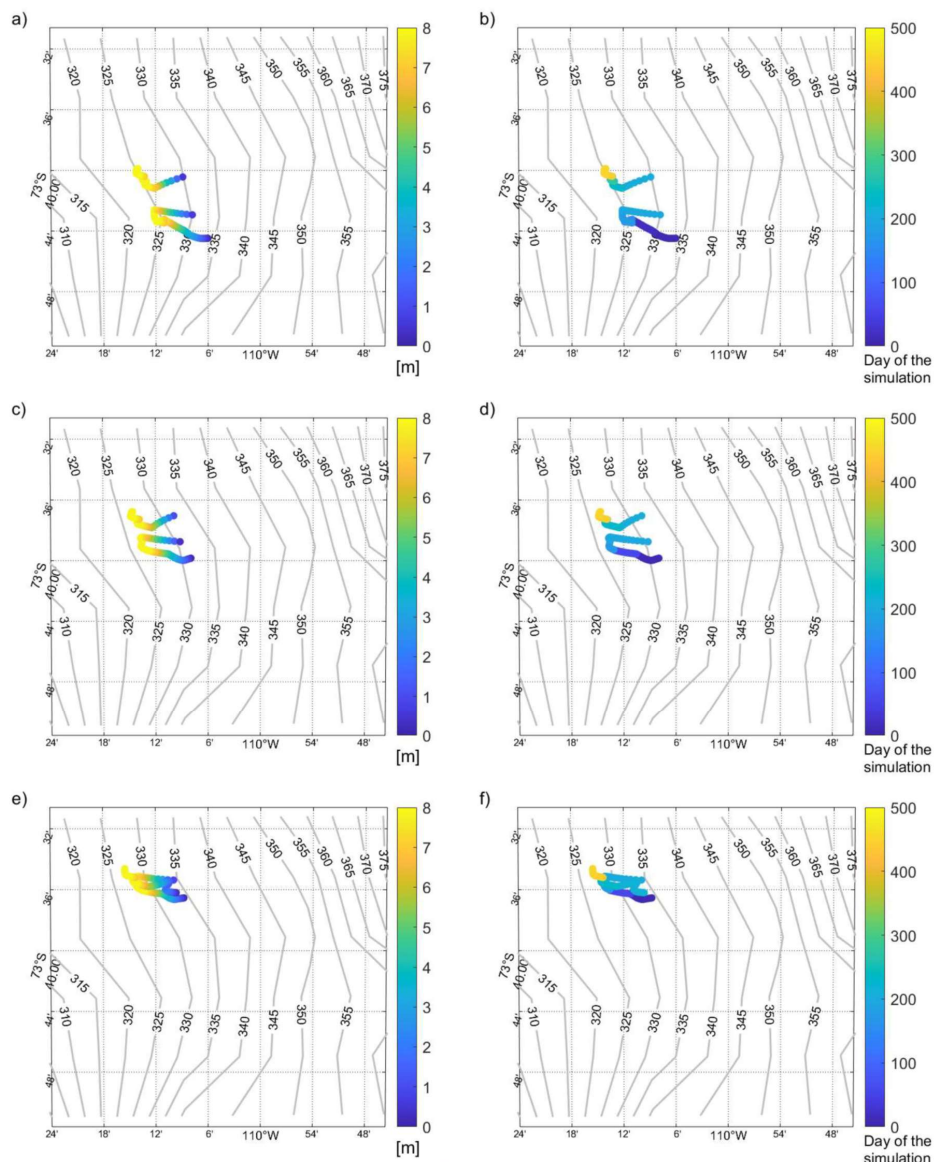
1151
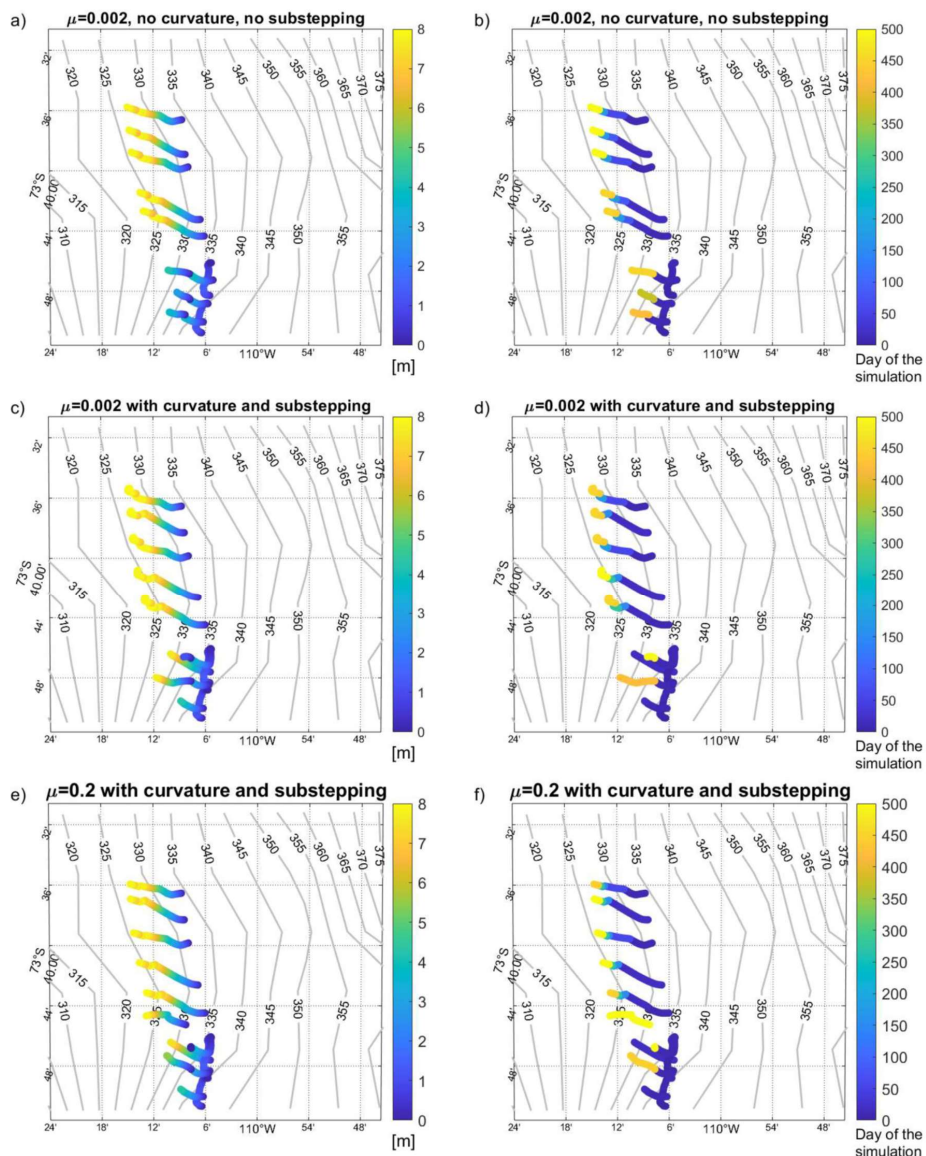
1152
Figure B1: As in Figure 11 but in simulations with a range of kinetic Coulomb coefficient values μ, sub-stepping choices, and representations of the topographic curvature effect.
1155
1156
1157

1158

Figure B2: As in Figure B1 but in simulations with zero Coulomb friction and 8-m sediment thickness. Each row represents an individual iceberg. The left column shows scour depths, and the right column shows their evolution in time during the LONG simulation with THICK icebergs.

We also probe the impact of temporal substepping. In the absence of sediment resistance forces, simulating the effect of gravity on grounded icebergs does require shorter timesteps and may necessitate substepping for iceberg dynamics. Here we present an important test of the iceberg substepping and its impact on gravitational acceleration/deceleration. In this test, we release a 97-m thick iceberg in an idealized rectangular basin that is not in a rotating frame of reference (the Coriolis force is set to zero). All wind/ocean/sea ice drag terms are set to zero. Iceberg melting is switched off, and so is solid-body friction. The sediment depth along the bottom is set to zero, eliminating any sediment resistance. Under these conditions, the only term remaining in the momentum balance is the gravitational disequilibrium term $\vec{a}_{gravity}$. The iceberg is initialized with south-eastward velocity above a sloping bottom whose depth decreases by 10m per 1 km in the southward direction, going from

41

1170   100m to 80m. As the iceberg moves up the bottom slope and out of free flotation, its kinetic energy is not dissipated but rather

1171   converted to potential energy. The gravity term should then convert this back into kinetic energy, accelerating the berg back

1172   down the slope, and this descent should exactly mirror the berg's ascent up the slope, like an idealized perfectly un-damped

1173   pendulum.

1174   We first test a case where the iceberg timestep equals the ocean timestep. The iceberg travels south-eastward up the

1175   slope, decelerating under gravity, and then reverses direction to slide north-eastward, accelerated by the same term. However,

1176   when the iceberg starts sliding back down the slope, its descent is not symmetric with respect to its initial ascent, despite the

1177   absence of external driving or dissipative forces (Figure B3); there is an asymmetry in the iceberg's meridional velocity going

1178   up the slope and coming back down (Figure B3).

1179   In our numerical tests, we found that this error is caused by an inadequate time-resolution of the iceberg deceleration

1180   and acceleration by the gravitational acceleration, which can be much larger than other sources in realistic cases. When we

1181   introduce temporal substepping within the iceberg module (four iceberg steps per one ocean step), we see a better symmetry

1182   between the iceberg's ascent and descent along the slope (Figure B3). This indicates an improved conservation of mechanical

1183   energy which is converted between kinetic and potential energy and this was found to be important in realistic cases.

1184

1185

1186

1187

1188

1189

1190

1191
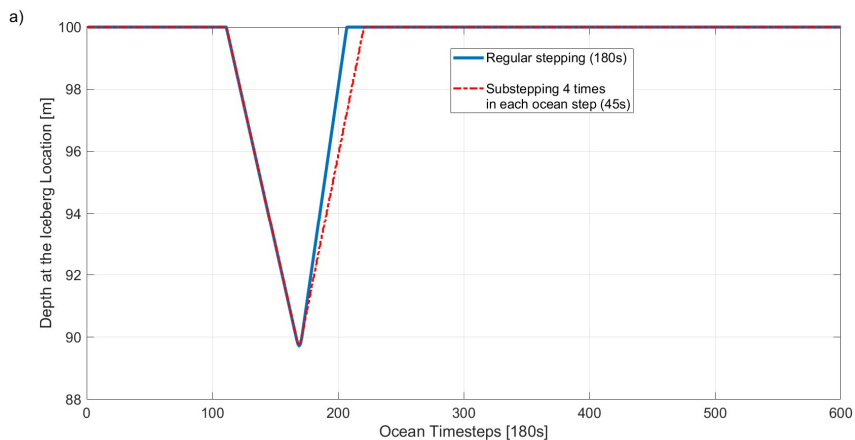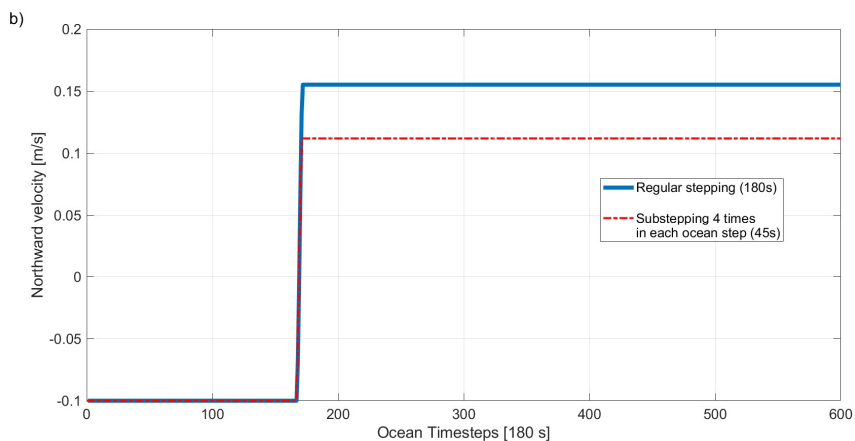
1192

1193

1194

1195

1196

1197

1198

1199

1200

1201

1202

1203

1204

Figure B3: Asymmetry between the ascent and descent (a); and deceleration and acceleration (b) of an iceberg along a frictionless slope with and without 1075 sub-stepping.

1207

1208

1209

1210

1211

1212

1213

1214

1215

1216

1217

1218

1219

1220

1221

1222

43

1223

1224   **Appendix C. Sea-ice drag on freely-floating and grounded icebergs**

1225   We calculate the average magnitude and orientation of the sea-ice drag for the case of freely-floating THICK and

1226   MEDIUM icebergs, as well as, kinetically grounded THICK icebergs. In the case of statically grounded icebergs, the solid-

1227   body friction and gravity are four orders of magnitude larger than the sea-ice contribution, and we do not consider that case

1228   here. Figure C1 highlights the different orientation of the sea-ice drag for freely-floating icebergs and grounded ones:. the drag

1229   projects onto the forward direction of motion of kinetically grounded icebergs.

1230
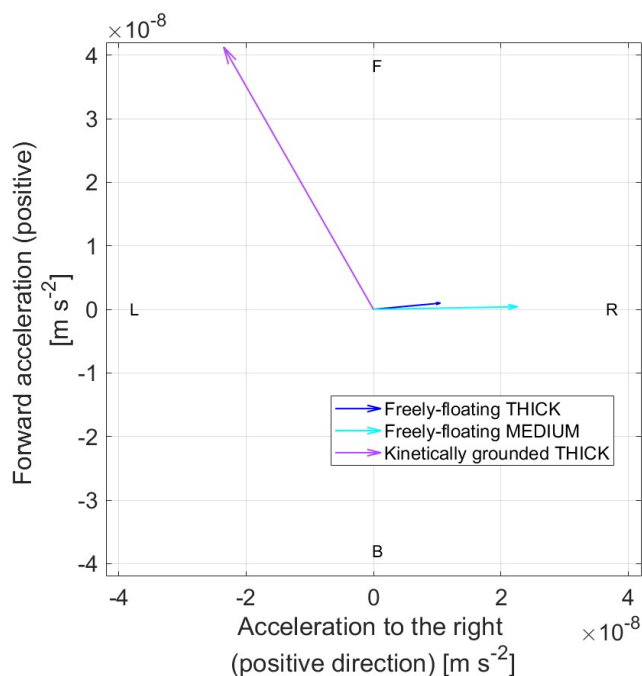
1231
1232   **Figure C1: As Figure 6f and 7f in the main text but for sea-ice drag on freely-floating THICK icebergs (dark blue), freely-floating**
1233   **MEDIUM icebergs (cyan), and kinetically-grounded THICK icebergs (purple).**

1234

1235

1236

1237

1238

1239

1240

1241

1242

1243

1244

1245

1246

1247 **Appendix D. Table of Symbols**

Symbol	Unit	Description
$\vec{a}_{ocean\ drag}$	ms^{-2}	Acceleration due to ocean drag
$\vec{a}_{atmos.drag}$	ms^{-2}	Acceleration due to atm. drag
$\vec{a}_{pressure\ gradient}$	ms^{-2}	Acceleration due to horizontal oceanic pressure gradient forces
$\vec{a}_{Coriolis}$	ms^{-2}	Acceleration due to Coriolis
$\vec{a}_{sea-ice\ drag}$	ms^{-2}	Acceleration due to sea-ice drag
$\vec{a}_{waves}$	ms^{-2}	Acceleration due to ocean waves
$\vec{a}_{sediment}$	ms^{-2}	Deceleration due to sediment resistance
$\vec{a}_{gravity}$	ms^{-2}	Acceleration due to gravity
$\vec{a}_{ground}$	ms^{-2}	Deceleration due to all forces active only on grounded icebergs
$\vec{a}_{solid}$	ms^{-2}	Deceleration due to solid-body friction
$\vec{a}_{static-solid}$	ms^{-2}	Deceleration due to solid-body friction in a static regime
$\vec{a}_{curvature}$	ms^{-2}	Effective horizontal acceleration due to topographic curvature
$\vec{a}_{net}$	ms^{-2}	Net acceleration
$\vec{a}_{net\ drivers}$	ms^{-2}	Acceleration due to all nondissipative forces
C_{drag}	m^{-1}	Drag coefficient parameter
$C_{drag-ocn}$	m^{-1}	Ocean drag coefficient parameter
$C_{drag-atm}$	m^{-1}	Atmospheric drag coefficient over icebergs
$C_{drag-atm-to-ocean}$	m^{-1}	Atmospheric drag coefficient over ocean
D	m	Scour depth
D_{keel}	m	Keel depth
f	s^{-1}	Coriolis parameter
g	ms^{-2}	Magnitude of the acceleration due to gravity
$\vec{g}$	ms^{-2}	Acceleration due to gravity
H_{Total}	m	Iceberg thickness
$H_{freeboard\ anom.}$	m	Iceberg freeboard anomaly (out of buoyancy-gravity equilibrium)
$\vec{k}$		Vertical direction
$L_{iceberg}$	m	Characteristic iceberg lengthscale
$M_{iceberg}$	kg	Iceberg mass
$\hat{n}$		Unit vector normal to the topographic plane
P	Pa	Ocean pressure

$\hat{s}$		Unit vector in the direction of the topographic slope
Δt	s	Timestep length
$\Delta \vec{u}$	ms^{-1}	Difference between the iceberg velocity and the velocity of the ambient ocean
$\vec{u}_{fluid}$	ms^{-1}	Velocity of ambient fluid
$\vec{u}_{atmos.}$	ms^{-1}	Atmospheric velocity
$\hat{u}$	ms^{-1}	Unit vector in the direction of the iceberg motion
W	m	Scour width
x, y, z		Horizontal dimenstions
α	rad	Angle of the trajectory relative to the horizontal plane
β	rad	Maximum local angle of the topographic slope
γ'	Nm^{-3}	Submerged unit weight
δ	m	Thickness of the Ekman layer
μ		Coefficient of Coulomb friction
μ_{static}		Coefficient of static Coulomb friction
ρ_0	$kg\ m^{-3}$	Reference density of ocean water
ρ_{sat}	$kg\ m^{-3}$	Saturated density of sediment
ρ_{water}	$kg\ m^{-3}$	Water density
ρ_{ice}	$kg\ m^{-3}$	Iceberg density
τ	$Pa\ (Nm^{-2})Pa$	Shear strength resistance of sediment
$\tau_{atm-ocean}$	$Pa\ (Nm^{-2})$	Magnitude of the wind stress at the ocean surface

1248